Water Vapor Transport and its Influence on Water Stable Isotope in Dongting Lake Basin

Xiong Xiao[1], Xinping Zhang[1,2]*, Zhuoyong Xiao[1], Zhongli Liu[1], Dizhou Wang[1],

Cicheng Zhang[1], Zhiguo Rao[1], Xinguang He[1,2], Huade Guan[3]

[1] *College of Geographic Science, Hunan Normal University, Changsha 410081, China*

[2] *Key Laboratory of Geospatial Big Data Mining and Applications in Hunan Province,*

Hunan Normal University, Changsha 410081, China

[3] *College of Science and Engineering, Flinders University, Adelaide SA 5001, Australia*

ABSTRACT: Understanding water vapor sources and transport paths is essential for assessing the water cycle and predicting precipitation accurately. Utilizing water vapor diagnosis and calculations, this study determined the water vapor sources and transport paths leading to precipitation in the Dongting Lake Basin in four seasons (represented by January, April, June, and October). In January, the water vapor generating precipitation originated from the Arabian Peninsula, driven by the southern branch of the westerlies over the southern side of the Tibetan Plateau, along the northern side of the Indian Peninsula through southwest China to reach the Dongting Lake Basin. In April, two transport paths emerged: one aligned closely with the January transport path but the location shifted slightly northward by one degree of latitude, and another was driven by the weak subtropical high over the southwestern Pacific, bringing moist air from the western Pacific via the South China Sea and Indochinese Peninsula. In June, the vapor sourced from the northern branch of the

---

* Corresponding author. Tel.: +86-13308486020; E-mail address: zxp@hunnu.edu.cn

South Indian Ocean subtropical high, crossed the equator and transported through various water bodies to southwestern China, finally reaching the basin. October saw a water vapor transport path from the western Pacific, crossing the South China Sea, and entering the Dongting Lake Basin influenced by the East Asian monsoon system. In different seasons, the variations in water stable isotopes along water vapor transport paths adhered to Rayleigh fractionation and water balance principles. These findings highlight the impact of atmospheric circulation on precipitation and isotopes, providing a framework for understanding water vapor isotope mechanisms and reconstructing past atmospheric conditions.

Keywords: Dongting Lake Basin; Water vapor sources; Transport paths; Precipitation isotopes; Precipitation amount.

Significance Statement

This research explores how water vapor transports and contributes to precipitation in the Dongting Lake Basin throughout different seasons. Understanding these paths is crucial because it helps us predict and manage water resources better, which is vital for agriculture, ecosystems, and communities relying on this water. By identifying the origins and paths of water vapor, we gain insights into how global climate patterns influence local weather. This knowledge is not only critical for accurate weather forecasting but also for preparing for future climate changes. Our findings highlight the complex interactions between the atmosphere and water cycle, offering a clearer picture of how seasonal shifts in atmospheric circulation impact regional precipitation patterns. This research explored how water vapor transports influenced the precipitation

isotopes in the Dongting Lake Basin in representative months of different seasons. By tracking water vapor from its source regions, we revealed the influence of large-scale atmospheric circulation on the transportation of water vapor to the Dongting Lake Basin. The changes in water stable isotopes along the water vapor transport paths highlighted the isotopic fractionation and water vapor exchange that occurred along these paths, while the isotopic changes in the precipitation reflect the cumulative influences of water vapor transport on the local precipitation. These comprehensive insights have clarified the influences of atmospheric circulation on water vapor transport and precipitation isotopes, and thus essential for predicting regional precipitation patterns.

1. Introduction

Diagnosing water vapor sources and analyzing water vapor transport are routine and foundational tasks, particularly within hydrometeorological services (Gimeno et al., 2020; Xu et al., 2020). A correct understanding of water vapor sources and transport is crucial for accurately evaluating the hydrological cycle and effectively predicting precipitation. For instance, in weather forecasting for the East Asian region, an essential condition for the occurrence of precipitation is the presence of sufficiently warm and moist air from low latitudes (Barker, et al., 2015; Tang et al., 2015; Hu et al., 2021). Moreover, the primary cause of meteorological drought in the East Asian monsoon region is often attributed to an anomalous decrease in water vapor sourced from the Bay of Bengal (He et al., 2022; Liu et al., 2023). Additionally, studies have shown that the abundance of stable isotopes in speleothems is related to monsoon intensity and is consequently linked to water vapor transport (Rao et al., 2013; 2016; Liang et al., 2020).

66   Over the past few decades, the employment of diverse mathematical models has

67   been the crucial approach to track~~ing~~ing and ~~deduce~~ deducing atmospheric water vapor

68   sources and transport paths (Gimeno et al., 2020; Xu et al., 2020; Pranindita et al., 2022;

69   Lekshmy et al., 2022). For instance, Pranindita et al. (2022) employed the water vapor

70   tracking model WAM-2layers to trace back the water vapor sources during heatwaves

71   in northern, western, and southern Europe, the reasons for the reduction of the local

72   precipitation can be attributed to a significant reduction in water vapor supply from the

73   North Atlantic due to anticyclonic patterns, along with the increased water vapor fluxes

74   from eastern Eurasia and local regions. Utilizing the Lagrangian model FLEXPART

75   v9.0, Pérez-Alarcón et al. (2023) identified precipitation water vapor sources associated

76   with the development of Indian Ocean tropical cyclones. Results showed that the water

77   vapor sources and transport mechanisms were different during different lifecycle stages

78   of tropical cyclones. Among numerous methods, the use of HYSPLIT for tracking water

79   vapor sources is widespread, which employs backward trajectory calculations and

80   atmospheric wind field information to derive water vapor transport trajectories at given

81   heights during a precipitation event, making it commonly used for tracing water vapor

82   during short-duration precipitation events (Draxler and Hess, 1998; Esquivel-

83   Hernández et al., 2019; Nie and Sun, 2022; Liu et al., 2023). However, due to inherent

84   model structure and tracking principles, derived water vapor transport paths at different

85   heights may vary or even be opposite. Moreover, this method cannot ascertain whether

86   the tracked water vapor indeed causes precipitation, nor can it provide information on

87   the magnitude of water vapor transport (Wu et al., 2015; Wu et al., 2022; Deng et al.,

88   2024).

89   With the continuous improvement of observational techniques and analytical

90   methods, utilizing reanalysis data to determine the water vapor sources that cause

91   precipitation has become a common practice (Sun et al., 2011; Hoffmann et al., 2019;

92   Guo et al., 2019; Shi et al., 2022). For instance, Sun et al. (2011) investigated the

93   climatic characteristics and decadal variations in water vapor transport in Eastern China

94   based on NCEP/NCAR reanalysis data from 1979 to 2009. The results revealed that the

95   variability in water vapor transport in the region is attributed to the combined influences

96   of the Indian summer monsoon and the East Asian summer monsoon. Based on the

97   dataset from ERA5 and isoGSM2, Xiao et al. (submitted) found a strong positive

98   correlation between seasonal precipitation and seasonal water vapor budget in the

99   Changsha region. They noted that southwestward water vapor transport contributes

100 significantly to water vapor input in all seasons, and only southwestward water vapor

101 flux exhibits a highly significant positive correlation with regional precipitation amount.

102 Despite the presence of water vapor input from the northwest direction, we observe no

103 correlation between the transport of water vapor from this direction and the regional

104 water vapor budget or precipitation amount. In some instances, an inverse relationship

105 is even apparent. These relationships imply that northwesterly winds do not exert a

106 direct influence on the precipitation generation in the region. Although water vapor

107 input from the northwest direction exists, there is no correlation between water vapor

108 transport in that direction and water vapor budget or precipitation amount, while it even

109 shows a negative correlation in some cases. Since the direction of water vapor transport

has an important influence on regional precipitation, it is necessary to reveal the influences of atmospheric circulation such as the water vapor source regions and water vapor transport paths, which determine the water vapor transport direction.

Water vapor transport controlled by atmospheric circulation not only determines precipitation events but also directly influences the precipitation isotopes, thus analyzing the water vapor sources and water vapor transport paths, as well as their influences on stable isotopes under different seasons, can elucidate the mechanisms influencing the atmospheric stable isotopes (Zhou et al., 2019; Dahinden et al., 2021; Zhan et al., 2023). For instance, Risi et al. (2010) conducted an analysis of water vapor and precipitation isotopes in the Sahelian region by combining water vapor budget and water vapor transport calculations, revealing that the isotopic composition of precipitation and atmospheric water vapor in the region is controlled by the intensity of air dehydration and changes in convection. Similarly, Sengupta et al. (2006) quantified the influences of different water vapor source regions on precipitation in the northern Indian monsoon region, finding that the isotopic composition of precipitation in the region is influenced by changes in water vapor source and atmospheric circulations over India. Moreover, Zhou et al. (2019) separately computed the correlations between $\delta^{18}O$ values of precipitation at different sites and found that during the prevalence of the summer monsoon (April to September) and winter monsoon (October to March), the key upstream regions influencing the precipitation isotopes in the Dongting Lake Basin located in south-central China ~~are~~ were the Bay of Bengal and southwestern China, respectively. However, as the critical regions influencing regional precipitation isotopes

may not necessarily be the water vapor source regions, these studies are yet to

definitively determine the water vapor source regions and water vapor transport paths.

Verifying whether the stable isotopic composition of water vapor undergoes

changes consistent with Rayleigh distillation during transport, and assessing the impact

of this transport on the isotopic composition of regional precipitation, constitute

significant research objectives. Existing studies indicate that in the East Asian monsoon

region, including the Dongting Lake Basin, differences in the water vapor sources and

transport direction during different seasons are the primary drivers of seasonal

variations in precipitation isotopes (Araguás-Araguás et al., 1998; Zhang et al., 2016;

Wei et al., 2018; Chiang et al., 2020). Typically, during the summer monsoon,

prevailing southeast or southwest winds dominate the East Asian monsoon region, with

water vapor for precipitation originating from low-latitude oceans (Barker, et al., 2015;

Wu et al., 2015; Tang et al., 2015), while precipitation isotopes are significantly

depleted influenced by intense rainout effects along the water vapor transport paths

during this period (Zhou et al., 2019; Wu et al., 2022). Conversely, during the winter

monsoon, northwest or northeast winds prevail in the East Asian monsoon region, ~~by~~

~~simple deduction,~~ the precipitation isotopes should be more enriched if water vapor for

precipitation is carried by westerlies or originates from the evaporation of inland

regions (e.g., Liu et al., 2011; Wu et al., 2015; Shi et al., 2021). However, both actual

observations from the Global Network of Isotopes in Precipitation (GNIP) and

simulations from isotope-enabled General Circulation Models (isoGCMs) consistently

demonstrate that, whether during the summer or winter monsoon, the spatial

distribution of precipitation isotopes in the East Asian monsoon region exhibits

significant latitudinal and continental effects—that is, the precipitation isotopes become

more depleted with the increases of latitude or distance from the ocean (Feng et al.,

2009; Zhang et al., 2012; Zhang et al., 2016). Consequently, the observed water vapor

transport during the summer monsoon aligns with the spatial distribution of

precipitation isotopes under the influence of latitudinal and continental effects and is

consistent with the Rayleigh distillation principle for water stable isotopes, however,

water vapor transport during the winter monsoon does not follow the above spatial

distribution and Rayleigh distillation principle (Tang et al., 2015; Zhou et al., 2019; Wu

et al., 2022).

Based on the understanding outlined above, a thorough investigation into the

seasonal variations in water vapor sources and transport paths for precipitation amount

and isotopes in the East Asian monsoon region is necessary, which may provide

significant benefit for accurately understanding regional hydrological mechanisms and

elucidating regional climate characteristics. Focusing on the Dongting Lake Basin

within the East Asian monsoon area, and drawing upon fundamental theories of

meteorology, water vapor diagnostics, and water vapor calculations, a broader spatial

understanding of the scientific issues surrounding water vapor transport can be

achieved,. this This study aims to (1) identify the water vapor sources and transport

paths contributing to the Dongting Lake Basin; (2) analyze the variations in

meteorological factors and water stable isotopes along the water vapor transport paths;

and (3) reveal the mechanisms by which water vapor sources and transport paths in the

176 monsoon region ~~influencing~~ influence precipitation amounts and isotopes.

2. Methods and materials

2.1 Study site

179   Dongting Lake Basin, situated in the south-central region of China (Fig. 1), is a

180 basin characterized by a subtropical monsoon climate, marked by distinct four seasons

181 and moderate humidity. Winters are wet and cold~~moist and cold~~, while summers are

182 warm and moist. Based on historical meteorological data from 1960 to 2017, the

183 Dongting Lake Basin experiences an average annual precipitation of 1375.6.0 mm.

184 During the colder months (October to March of the following year), precipitation is

185 relatively low due to the influence of continental air masses. However, from late April

186 onward, influenced by ~~maritime~~oceanic monsoons, precipitation increases significantly,

187 accompanied by a notable rise in temperature, with precipitation predominantly

188 occurring from April to June (Liu et al., 2023; Xiao et al., 2024).
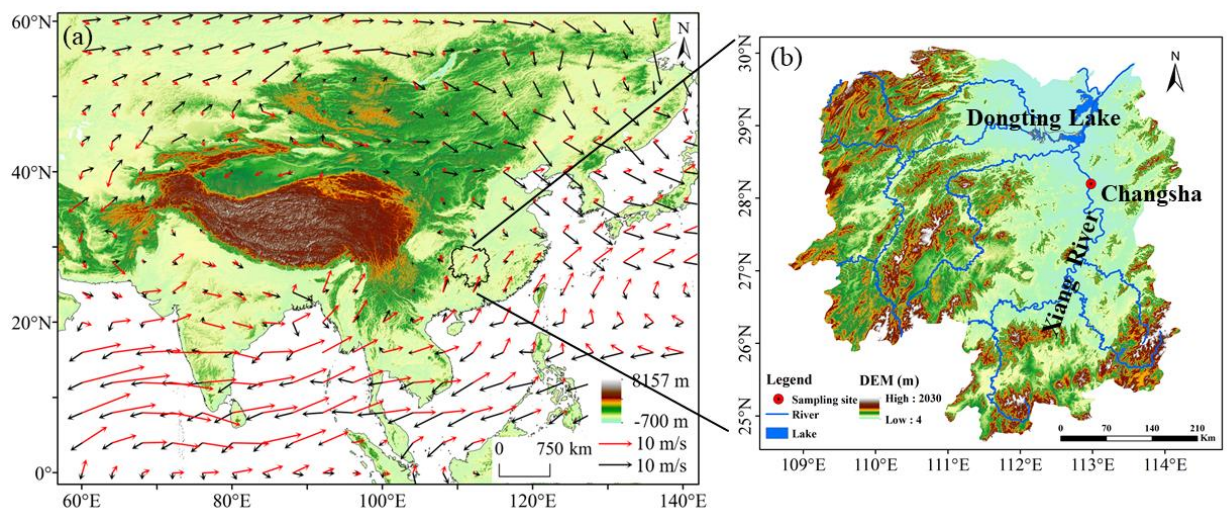
190   Fig. 1 Map showing the location of the Dongting Lake Basin, and the Changsha

191   sampling site in the East Asian Monsoon Region. Note that the black arrow and red

192   arrow in subplot (a) represent the average wind field at 850 hPa in January and June,

193           respectively.

194  The prevailing wind refers to the wind or wind direction that appears the most

195 frequently in a region during a specific period. Its occurrence is closely related to the

196 changes in the average atmospheric circulation conditions due to the thermal

197 differences between land and sea~~the atmospheric circulation of the region~~. In the East

198 Asian monsoon region, which includes the Dongting Lake Basin, the strong cold high-

199 pressure system influences the winter season, resulting in prevailing northerly winds

200 ~~near~~ at the lower troposphere~~surface~~, with northwesterly winds prevailing in the basin

201 as shown by the average wind field at the 850 hPa in January, i.e. the black arrow in

202 Fig. 1a. In the summer, influenced by the Western Pacific Subtropical High and the

203 Indian Low, the ~~near-surface~~ winds at the lower troposphere are predominantly

204 southerly in the East Asian monsoon region, with southwesterly winds prevailing in the

205 Dongting Lake Basin as shown by the average wind field at the 850 hPa in June, i.e.

206 the red arrow in Fig. 1a. Positioned at the convergence of the prevailing northerly winds,

207 prevailing southerly winds, and westerly winds, the Dongting Lake Basin experiences

208 complex precipitation processes and different precipitation amounts in different seasons

209 and water vapor transport directions. This complexity results in high variability in the

210 precipitation isotope ~~dynamics~~ (Zhou et al., 2019; Xiao et al., 2024).

211 **2.2 Water samples collection and measurement~~analysis~~**

212  From January 1, 2010 to December 31, 2022, precipitation sample sampling has

213 been conducted at the Meteorological Garden of Hunan Normal University in Changsha

214 (28°11'N, 112°56'E). The sampling protocol followed the meteorological observation

standards of China's meteorological departments, with samples collected at 08:00 and 20:00 Beijing time on precipitation days. Liquid precipitation was directly collected in sealed 30 ml polyethylene bottles after measuring the precipitation amount, while solid precipitation was first collected in air-tight plastic bags, then measured for meltwater volume after natural melting, and transferred to the same size polyethylene bottles. All the collected water samples were stored in a refrigerator at 0°C before testing.

Precipitation sample analysis from 2010 to 2013 was conducted using a Liquid Water Isotope Analyzer (DLT-100, Model: 908-0008) from Los Gatos Research, USA; subsequently, a new generation Liquid and Gas Dual-Mode Stable Isotope Analyzer (IWA-35EP, Model: 912-0026-1000) from the same company was used from 2014 to 2022. The oxygen and hydrogen stable isotope ratio in the water samples were expressed in per mil (‰) deviations relative to the Vienna Standard Mean Ocean Water (V-SMOW), calculated using the equation:

$$\delta^2 H \text{ or } \delta^{18} O = \left[R_s \middle/ R_{\text{V-SMOW}} - 1 \right] \times 1000 \tag{1}$$

In the equation, R_s and $R_{\text{V-SMOW}}$ represent the oxygen (or hydrogen) stable isotope ratios $^{18}O/^{16}O$ (or $^2H/^1H$) in the water sample and in Vienna Standard Mean Ocean Water (V-SMOW), respectively. The testing precision averaged $\delta^{18}O \leq 0.3‰$ and $\delta^2 H \leq 2‰$ during 2010-2013, and $\delta^{18}O \leq 0.2‰$ and $\delta^2 H \leq 0.6‰$ during 2014-2022. If there were two precipitation samples in one day, the precipitation stable isotope values for that day were represented by the volume-weighted average. In total, 1668 precipitation days' $\delta^{18}O$ ($\delta^2 H$) data were obtained over the past 13 years.

2.3 Ancillary data

237   ERA5, produced and released by the European Centre for Medium-Range Weather

238   Forecasts (ECMWF), is the fifth-generation global atmospheric reanalysis data product

239   from the center. Compared to its predecessor ERA-Interim, ERA5 incorporates a state-

240   of-the-art integrated forecasting system, integrates more historical observational data,

241   and reprocesses a large amount of assimilation data, resulting in significantly improved

242   accuracy (Albergel et al., 2018; Hoffmann et al., 2019). Additionally, ERA5 features

243   substantial improvements in temporal and spatial resolution. The temporal resolution

244   has increased from 6 hours in ERA-Interim to 1 hour, while the horizontal resolution

245   has improved from 79 km to 31 km, and the highest vertical extension reaches 0.01 hPa

246   ~~altitude~~level. These enhancements enable ERA5 to capture finer atmospheric details.

247   Moreover, the number of variables provided by ERA5 has increased from over 100 in

248   ERA-Interim to the current 240, and the ~~data~~ release delay days of ERA5 ~~has~~ have been

249   reduced from 2-3 months in ERA-Interim to 5 days (Albergel et al., 2018; Hoffmann et

250   al., 2019). The reanalysis data used in this study include surface pressure (p_s, hPa),

251   ~~specific humidity at 1000/850/700/600/500/400/300 hPa, altitudinal wind, and~~

252   ~~meridional wind~~potential height of 500 hPa (H_{500}, meter), and specific humidity (q,

253     $kg \cdot kg^{-1}$), latitudinal wind (m/s), and meridional wind (m/s) at

254   1000/850/700/600/500/400/300 hPa. The horizontal resolution is 1°×1°, with a

255   temporal step of 1 hour. This dataset was used to calculate the vertical integral of water

256   vapor fluxes into a specified region, introduced in section 2.4.

257   Since the direct observation of the isotopic fractionation process in the atmosphere

258   is extremely challenging~~the fractionation process of water stable isotopes in the~~

atuosphere cannot be directly observed, analyzing the variations of atmospheric stable isotopes requires the application of stable isotopes fractionation theory along with the fundamental principles and methods of meteorology. In terms of research methods, the introduction of atmospheric circulation models for water stable isotope cycling, such as isoGCMs, provides a unique and effective tool. Among numerous isoGCMs, isoGSM (Isotope-incorporated Global Spectral Model) exhibits relatively good simulation performance in the East Asian region (Zhang et al., 2020; Kathayat et al., 2021). isoGSM is a stable isotope GCM developed by Yoshimura et al. (2008), which integrated water isotope cycling and fractionation processes into the Global Spectral Model at the Scripps Experimental Climate Prediction Center. The driving factors data include sea surface temperature, sea ice, and temperature and horizontal wind fields in 28 vertical layers. This model addresses the Gibbs phenomenon in atmospheric circulation models and performs better in simulating water vapor transport processes in arid and high-altitude regions (Yoshimura et al. 2008; Bong et al., 2024). The second-generation isoGSM2 has a higher temporal and spatial resolution in simulating water vapor and precipitation isotopes compared to the first-generation (Chiang et al., 2020). It utilizes the NECP-R2 (National Centers for Environmental Prediction Reanalysis 2) reanalysis dataset and abandons the NDSL (Non-iteration Dimensional-split Semi-Lagrangian) advection scheme used in the previous generation. By dynamically correcting the model output using reanalysis data, isoGSM2's simulation results are closer to actual atmospheric conditions, thereby improving the accuracy of water vapor and precipitation isotope simulations (Bong et al., 2024).

281   The water stable isotope simulation data used in this study are from isoGSM2

282   (January 1979 to December 2017, totaling 468 months), including monthly

283   precipitation amount (P, mm), stable isotopes (δ^2H and $\delta^{18}O$) in the precipitation and

284   vertical integral of water vapor (~~δ^2H_v, $\delta^{18}O_v$,~~ δ^2H_p, ~~and~~ $\delta^{18}O_p$, δ^2H_v, and $\delta^{18}O_v$), and

285   the calculated deuterium excess in water vapor and ~~in~~ precipitation (Ex_d_v and Ex_d_p).

286   The spatial scale ranges from 30°S to 70°N and 0° to 280°E, with a horizontal resolution

287   of 1°×1° (Chiang et al., 2020; Liu et al., 2023).

2.4 ~~**Model Analysis**~~**Calculation of the Vertical Integral of Water Vapor Flux Q**

289   The water vapor transport flux serves as a metric for both the magnitude and

290   direction of water vapor transport, representing the mass of water vapor passing through

291   a unit cross-section per unit of time (Sun et al., 2011). The specific calculation equation

292   is as follows:

$$Q = \frac{1}{g}\int_{p_t}^{p_s} Vq\,\mathrm{d}p \tag{2}$$

294   Where the meridional component Q_λ and the latitudinal component Q_φ of the water

295   vapor transport flux are given by:

$$Q_\lambda = \frac{1}{g}\int_{p_t}^{p_s} uq\,\mathrm{d}p \tag{3}$$

$$Q_\varphi = \frac{1}{g}\int_{p_t}^{p_s} vq\,\mathrm{d}p \tag{4}$$

298   Here, Q represents the vertical integral of water vapor flux ($kg \cdot m^{-1} \cdot s^{-1}$), including the

299   meridional component Q_λ and the latitudinal component Q_φ. V denotes the vector wind

300   speed ($m \cdot s^{-1}$), including the latitudinal wind speed (v) and meridional wind (u), q

301   represents specific humidity ($kg \cdot kg^{-1}$), g is the acceleration due to gravity ($m \cdot s^{-2}$), p_s is

302 the lower boundary pressure (hPa), and p_t is the upper boundary pressure (hPa). In the

303 actual atmosphere, water vapor content above 300 hPa is minimal, thus p_t is set to 300

304 hPa when calculating the vertical integral of water vapor flux through the entire

305 atmospheric column.

306 **3. Results**

307 **3.1 Seasonal Variation Characteristics of Precipitation Isotopes in the Changsha**

308 **Region**

309 The monthly weighted average and total monthly calculations were performed on

310 the daily $\delta^{18}O_p$, daily Ex_d_p, and daily P collected from the Hunan Normal University

311 and the Changsha National Meteorological Reference Station, yielding the seasonal

312 variations of multi-year monthly weighted average $\delta^{18}O_p$, monthly weighted average

313 Ex_d_p, and monthly average P in the Changsha region (Fig. 2a). The $\delta^{18}O_p$, Ex_d_p, and

314 P in Changsha exhibited significant seasonal variations—that is, the maximum value

315 of $\delta^{18}O_p$ appeared in March and April, both at −3.576‰, but did not correspond to the

316 months with the lowest precipitation amounts. The three lowest values of $\delta^{18}O_p$

317 occurred in July, August, and September, respectively at −9.455‰, −8.93‰, and

318 −9.42‰, with a simple arithmetic average of −9.273‰, which also did not correspond

319 to the months with the highest precipitation amounts. The maximum value of Ex_d_p

320 (20.051‰) appeared in January, and the minimum value (9.293‰) appeared in August,

321 both of which were months with relatively low precipitation. Due to these significant

322 differences in the phases of precipitation isotopes and amounts, it is apparent that

323 explaining the variations in local precipitation stable isotopes solely based on the

seasonal variations in local precipitation amounts is insufficient.
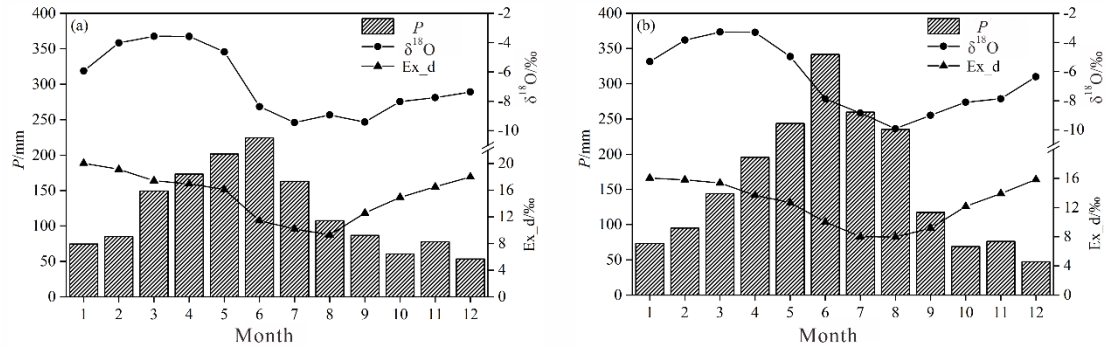
Fig. 2 Comparisons between seasonal variations of precipitation $\delta^{18}O$ ($\delta^{18}O_p$),

precipitation ~~excess~~ deuterium excess (Ex_d_p), and precipitation amount (P) measured

at the Changsha station (a) and simulated by isoGSM2 or driven from the ERA5

reanalysis dataset at the corresponding grid (b).

Monthly weighted average calculation was performed on the monthly $\delta^{18}O_p$ and

Ex_d_p simulated by isoGSM2 at the Changsha grid, and the monthly average

calculation was performed on the P from ERA5, yielding the seasonal variations of

simulated monthly weighted average $\delta^{18}O_p$ and Ex_d_p and ERA5 monthly average P at

the Changsha grid (Fig. 2b). The simulated and calculated $\delta^{18}O_p$, Ex_d_p, and P in

Changsha all effectively reproduced the seasonal variations of the corresponding

observations. The root mean square errors (RMSE) between simulated and observed

values were 0.5~~4~~‰, 2.7~~88~~‰, and 59.7 mm, respectively. Corresponding to the

observed seasonal variations, the two maximum values of the simulated $\delta^{18}O_p$ occurred

in March and April, at −3.2~~93~~‰ and −3.3~~1~~‰, respectively, with very small differences

from the observed values. The three lowest values of simulated $\delta^{18}O_p$ also occurred in

July, August, and September, at −8.8~~4~~‰, −9.9~~2~~‰, and −9.0~~0~~‰, respectively, with a

simple arithmetic average of −9.2~~53~~‰, which was consistent with the observed values.

The maximuuum value of simulated Ex_d$_p$ (16.051‰) appeared in January, and the

minimum value (7.978.0‰) appeared in August (Fig. 2b), both consistent with the

observed values (Fig. 2a). These comparisons indicated that isoGSM2 exhibited strong

capabilities in simulating the spatial distribution and temporal variations of atmospheric

water stable isotopes.

To analyze the seasonal variation in the atmospheric water vapor transport and its

influences on the regional precipitation isotopes, and taking into account the hydro-

climatic characteristics of the study region (Fig. 2), four representative months

including January, April, June, and October were selected as the study seasons. Among

these representative months, January in the Changsha region represents winter,

characterized by the lowest temperatures and relatively low precipitation throughout

the year. April signifies spring, with rapidly increasing precipitation amounts and

frequent fluctuations between warm and cold air masses. June represents the peak of

the summer monsoon season, with the highest monthly precipitation amount of the year.

October represents autumn, characterized by clear and cool weather and the second-

lowest precipitation throughout the year under the influence of the West Pacific

Subtropical High.

3.2 Water Vapor Transport in the Dongting Lake Basin in Different Seasons

3.2.1 Average Water Vapor Transport Path in the Dongting Lake Basin in January

Based on the ERA5 reanalysis data, we calculated and plotted the spatial

distribution of the 500 hPa average geopotential height (H_{500}) and average Q (Fig. 3a),

multi-year average P (Fig. 3b) in January. Moreover, based on the isoGSM2 simulation

365   data, we plotted the spatial distributions of the average $\delta^{18}O_v$ (Fig. 3c), $\delta^{18}O_p$ (Fig. 3d),

366   Ex_d_v (Fig. 3e), and Ex_d_p (Fig. 3f) in January.

367
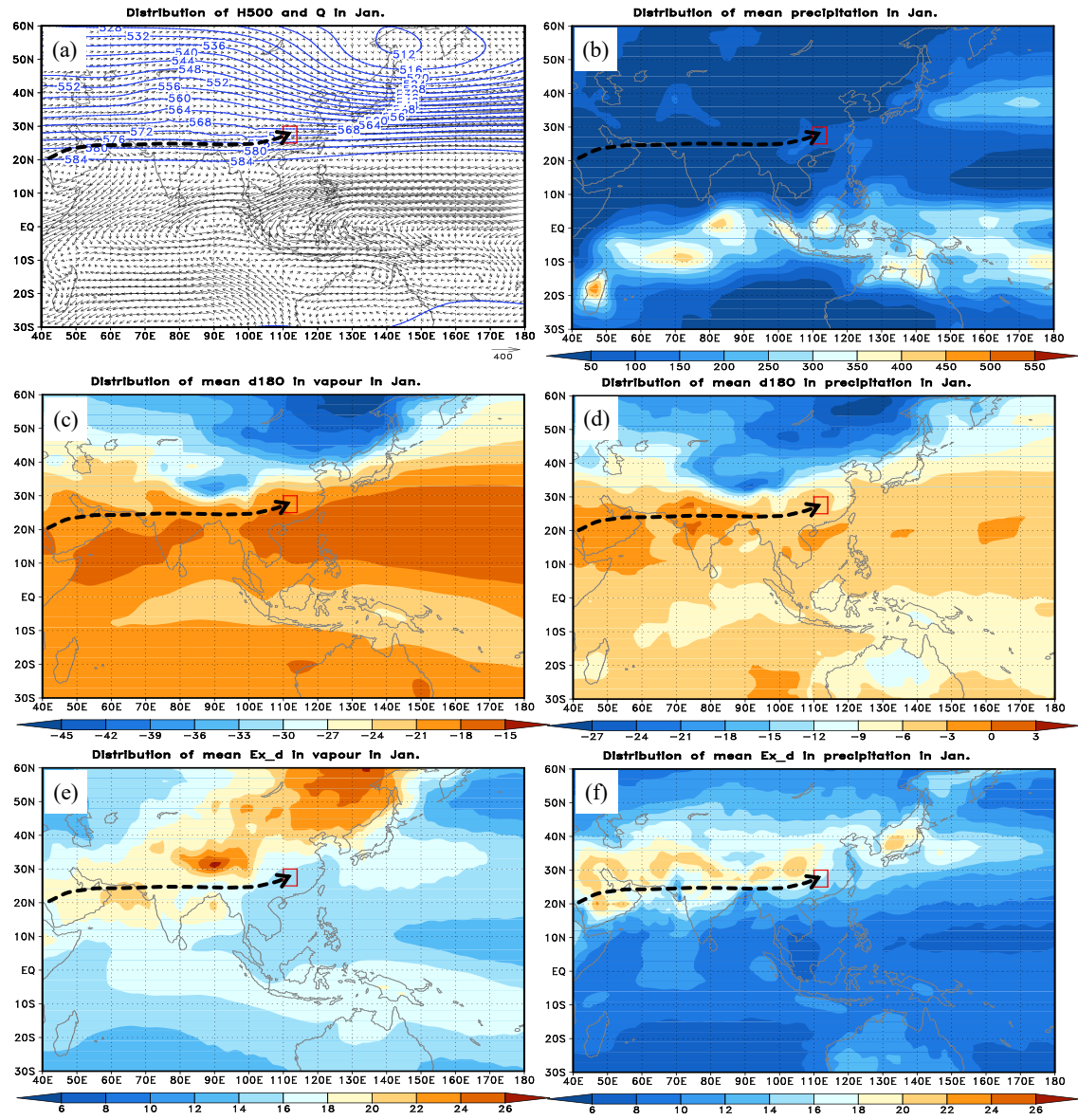
368   Fig. 3 Mean vapor transport path to the Dongting Lake Basin and the spatial

369   distributions of Q with H_{500} (a), P (b), $\delta^{18}O_v$ (c), $\delta^{18}O_p$ (d), Ex_d_v (e), and Ex_d_p (f) in

370   January. Q, H_{500}, P, $\delta^{18}O_v$, $\delta^{18}O_p$, Ex_d_v, and Ex_d_p represent the vertical integral of

371   water vapor flux, 500 hPa average geopotential height, precipitation amount, $\delta^{18}O$ in

372   atmospheric water vapor and precipitation, and deuterium excess in atmospheric

373   water vapor and precipitation, respectively, hereinafter the same.

374   At the H_{500} field of East Asia, the deep East Asian Trough was stably located along

375   the East coast, and the strong Ural Ridge in the mid-high latitudes of 70°E to 90°E (Fig.

376   3a). Influenced by the northwest airflow behind the trough and ahead of the ridge, the

377   northwest winds prevailed in most parts of East Asia. In the Dongting Lake Basin

378   (highlighted in the red box in Fig. 3), influenced by the middle-latitude westerly belt,

379   water vapor transport mainly was from west to east. Under the control of the cold

380   continental high, precipitation was relatively low over the entire East Asia and South

381   Asia, while the regions with high P values were mainly distributed in the equatorial

382   convergence zone and the North Pacific located ahead of the East Asian Trough (Fig.

383   3b). Unlike most regions of the East Asian continent, the Dongting Lake Basin was

384   situated~~lied~~ on a wet tongue, benefiting from the Southwest Vortex in the eastern

385   Tibetan Plateau (Lai et al., 2023; Huang and Li, 2023). This Southwest Vortex is a

386   cyclonic bypass flow of westerlies from the southern branch of the Tibetan Plateau, as

387   this vortex moves eastward with the westerly belt, it brings precipitation to the

388   downstream areas

389   The $\delta^{18}O_v$ and $\delta^{18}O_p$ in January exhibited significant continental effects (Figs. 3c

390   and 3d). Under the control of continental cold air masses, the centers of minimum $\delta^{18}O_v$

391   and $\delta^{18}O_p$ values were located in the mid-high latitudes of Eastern Siberia. Due to the

392   influence of topography, the $\delta^{18}O_v$ tended to be negative over the Tibetan Plateau. These

393   two low-value regions correspond to the cold pole of Eurasia and the Earth's third pole,

394   respectively. Regions enriched in atmospheric water isotopes were mainly distributed

395   over vast oceans and Western Asia. In the equatorial convergence zone, due to the

rainout effects, both water vapor isotopes and precipitation isotopes were depleted to some extent. Along with the surrounding the Dongting Lake Basin, the abundance of water vapor isotopes and precipitation isotopes in the Dongting Lake Basin were comparable to those of the middle-low latitude oceans in January.

The spatial distributions of the Ex_d_v and Ex_d_p exhibited the characteristics of low in the ocean and high in the land, but the regions where their maximum values occurred did not completely correspond (Figs. 3e and 3f). The maximum value of the Ex_d_v mainly appeared in Eastern Siberia and the Tibetan Plateau, showing a meridional distribution from northeast to southwest, while the high values of the Ex_d_p mainly occurred in mid-latitude inland regions, showing a latitudinal distribution from west to east. The Ex_d_v and Ex_d_p values in the Dongting Lake Basin lay exactly in the transition region from low to high values. Typically, the Ex_d_p largely depended on the Ex_d_v, but processes such as condensation and super-saturation in ice-water mixed clouds, secondary evaporation below clouds, evaporation from underlying surfaces, and the exchange and diffusion of water vapor isotopes could cause precipitation isotopes to deviate to varying degrees from atmospheric water vapor isotopes (Zhang et al., 2016)Typically, the Ex_d_p largely depended on the Ex_d_v, but processes such as condensation in clouds, secondary evaporation below clouds, evaporation from underlying surfaces, and the exchange and diffusion of water vapor isotopes could cause precipitation isotopes to deviate to varying degrees from atmospheric water vapor isotopes (Zhang et al., 2016).

In the Q field (Fig. 3a), regarding the Dongting Lake Basin as the endpoint, the

418   vector cluster of the vertical integral of water vapor flux (i.e., the Q) directed towards

419   the Dongting Lake Basin delineates the path of water vapor transport in January (black

420   arrow lines in Fig. 3). The water vapor transport path was determined by the rules to

421   find the systematic vapor currents in the Q field, which need to have the same

422   directionality and draw the path along the central axis of the vapor currents. The source

423   regions of water vapor were determined based on the conditions for the formation of

424   air masses, which need to form on a uniform underlying surface and possess stably in

425   terms of isotopic, thermodynamic, and dynamic properties as well as circulation

426   condition, typically located over vast land and ocean regions (Smirnov and Moore,

427   1999)a vector interpolation method was applied regarding the Changsha site as the

428   endpoint, as well as based on the drawing of streamlines, the average water vapor

429   transport path in January was obtained (black arrow lines in Fig. 3). This transport path

430   originated near the Arabian Peninsula. Driven by the southern branch of the westerly

431   stream jet on the southern side of the Tibetan Plateau, water vapor transported along the

432   southern side of the Tibetan Plateau, passed through southwestern China via the

433   northern part of the Indian Peninsula, and reached the Dongting Lake Basin. It can be

434   seen that this water vapor transport path was not consistent with the prevailing wind

435   direction in January as shown in Fig. 1a, which was represented by the black arrows

436   with northwesterly winds prevailing in the Dongting Lake Basin as shown by the

437   average wind field at the 850 hPa.

438   Six series of factors at the grid points along the water vapor transport path were

439   derived from each factor field in January, including the variations of Q, P, $\delta^{18}O_v$, $\delta^{18}O_p$,

Ex_d_v, and Ex_d_p. Moreover, the grid points along the water vapor transport path were identified on the central axis of the path and based on the principle of uniform distribution of the scatter points, and the factors at the grid points were obtained from these scatter points. Besides, the factors at the grid points along the water vapor transport path exhibit, in spatial terms, average characteristics of conditions over multiple years, and, in temporal terms, sequential characteristics of these factors along the water vapor transport path. As shown in Fig. 4, both the Q and P were relatively low, while increased to some extent due to the converging effect of Southwest Vortex after entering the Dongting Lake Basin (Figs. 4a and 4b). Under the weak atmospheric meridional disturbances in January, the changes in $\delta^{18}O_v$ and Ex_d_v were minor, fluctuating slightly around −19.~~0~~1‰ and 18.~~1~~2‰, respectively (Figs. 4c and 4e). Due to the low precipitation amount, the $\delta^{18}O_p$ values were ~~relatively positive~~higher in the first half of the water vapor transport path, and then became more negative in the latter half with the enhanced rainout effect, while the Ex_d_p became more positive (Figs. 4d and 4f).
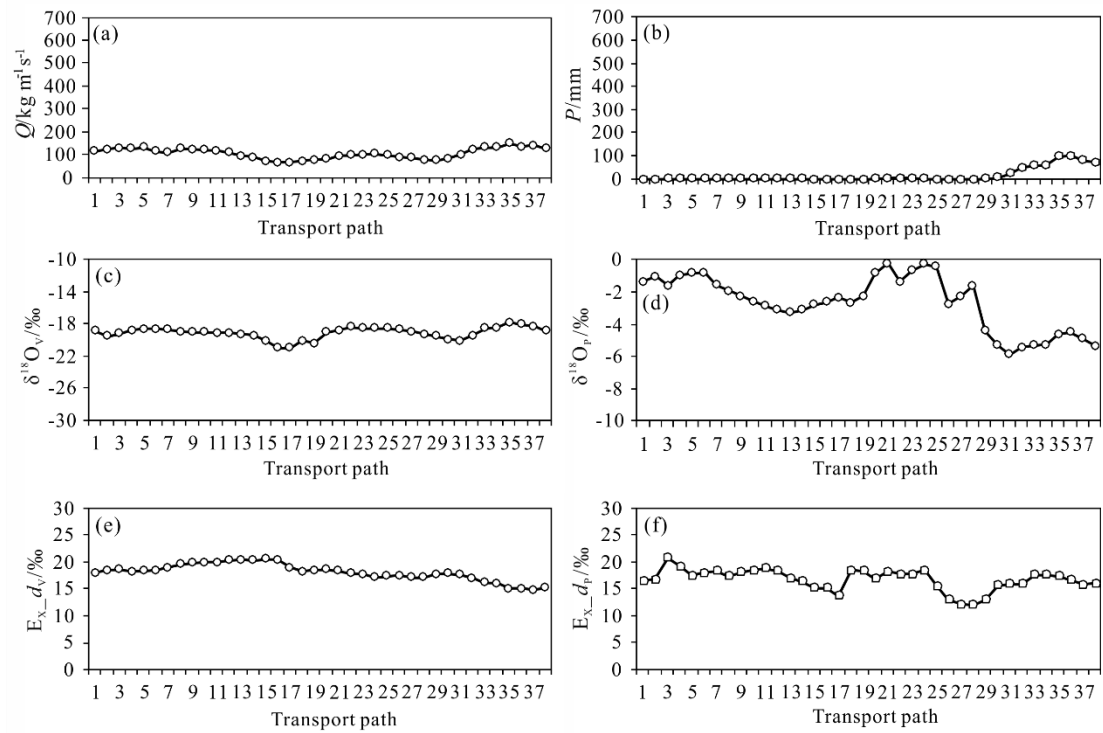
Fig. 4 Mean variations of Q (a), P (b), $\delta^{18}O_v$ (c), $\delta^{18}O_p$ (d), Ex_d_v (e), and Ex_d_p (f)

along the vapor transport path in January

3.2.2 Average Water Vapor Transport Path in the Dongting Lake Basin in April

Based on the ERA5 reanalysis data and the isoGSM2 simulation data, the spatial

distributions of H_{500}, Q, P, $\delta^{18}O_v$, $\delta^{18}O_p$, Ex_d_v, and Ex_d_p were calculated and plotted

in April (Fig. 5). At the H_{500} field (Fig. 5a), the East Asian Trough and Ural Ridge were

still present in the mid-to-high latitudes. The mid-to-high latitude regions of East

Asia~~The East Asian mid-to-high latitude regions~~ were still influenced by the winter

monsoon, while its intensity was significantly weakened. In the mid-to-low latitudes,

the Western Pacific subtropical high has strengthened and expanded northward, with

the ridge line located approximately near 15°N. A shallow trough appeared in the

northern part of the Bay of Bengal, indicating the beginning of tropical systems

influencing the mid-to-low latitude regions of East Asia. In the Dongting Lake Basin,

influenced by the westerlies and low-latitude atmospheric systems, the water vapor transport shifted to the domination by the southwestward direction. Most continental regions of East Asia and South Asia experienced a certain degree of precipitation increase, with the rainy band caused by the intertropical convergence zone, previously located in the Southern Hemisphere, moving to the Northern Hemisphere (Fig. 5b). The Dongting Lake Basin also entered the spring flood season in April, while the Changsha region was situated in a center with an above-average spring precipitation amount compared to the surrounding regions in this period (Fig. 5b).
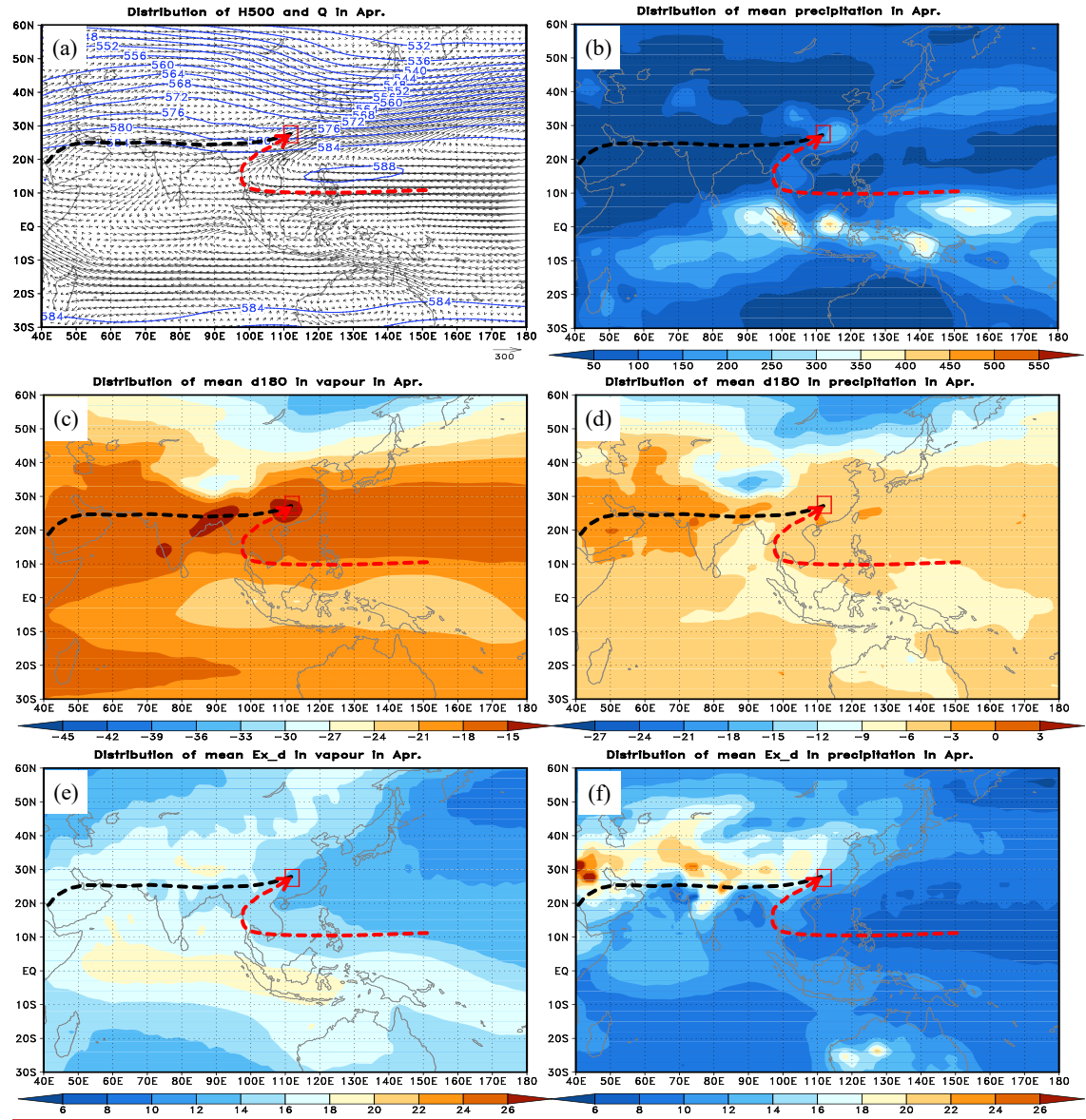
Fig. 5 Mean vapor transport paths to the Dongting Lake Basin and the spatial

distributions of Q with H_{500} (a), P (b), $\delta^{18}O_v$ (c), $\delta^{18}O_p$ (d), Ex_d$_v$ (e), and Ex_d$_p$ (f) in

April.

Compared to the situations in January, there were no major changes in the spatial

distributions of $\delta^{18}O_v$ and $\delta^{18}O_p$ in April (Figs. 5c and 5d). In the regions with low $\delta^{18}O_v$

and $\delta^{18}O_p$ values, previously located in Eastern Siberia and the Tibetan Plateau,

atmospheric stable isotopes have significantly enriched. Due to temperature rise and

enhanced evaporation, the regions with high levels of $\delta^{18}O_v$ and $\delta^{18}O_p$ in the mid-to-

486 low latitudes showed continual increases in the $\delta^{18}O_v$ and $\delta^{18}O_p$ values. With the

487 strengthening of water vapor convergence in the Dongting Lake Basin, the $\delta^{18}O_v$ in the

488 Dongting Lake Basin showed significant increases in April, leading to an isotopic

489 enrichment in precipitation. Compared to the large-scale region, the water isotope

490 composition in the Dongting Lake Basin, was not significantly different from that of

491 the mid-to-low latitude ocean, indicating the controls by the ~~maritime~~oceanic air masses

492 (Figs. 5c and 5d).

493   In April, the spatial distributions of Ex_d$_v$ and Ex_d$_p$ were comparable to the

494 situations in January (Figs. 5e and 5f). The regions with high-value Ex_d$_v$, previously

495 located in Eastern Siberia and the Tibetan Plateau, respectively, showed significant

496 reductions in range and intensity, but the regions with low-value Ex_d$_v$ in the Western

497 Pacific expanded, thereby reducing the differences between land and sea. With the

498 continuous inland influx of ~~maritime~~oceanic water vapor from the Western Pacific

499 Ocean, the range of low-value regions of the Ex_d$_p$ has expanded. Influencing by the

500 increasing precipitation, the range of high-value regions of the Ex_d$_p$ in mid-latitude

501 inland regions has narrowed, but the intensity has increased to varying degrees,

502 especially in West Asia. Finally, both the Ex_d$_v$ and Ex_d$_p$ in the Dongting Lake Basin

503 showed decreases, which were influenced by the gradually strengthening summer

504 monsoon and the situation of water vapor transport (Figs. 5e and 5f).

505   ~~Based on the vector interpolation method, t~~Two water vapor transport paths were

506 obtained according to the vector interpolation method introduced in section

507 3.2.1~~regarding the Changsha site as the endpoint~~ (Fig. 5a). The first water vapor

508 transport path—that is, ~~the~~ Path I (represented by black arrow lines in Fig. 5), was

509 essentially consistent with the water vapor transport path in January, but it is slightly

510 shifted northward by one degree of latitude. The second water vapor transport path—

511 that is, Path II (represented by red arrow lines in Fig. 5), driven by the weak Western

512 Pacific subtropical high, guided warm and moist water vapor from the low latitudes of

513 the Western Pacific along the outer edge of the subtropical high, passing through the

514 South China Sea and the Indochinese Peninsula and finally reached into the Dongting

515 Lake Basin. Corresponding data at the grid points along two water vapor transport paths

516 were extracted and plotted for the Q, P, $\delta^{18}O_v$, $\delta^{18}O_p$, Ex_d_v, and Ex_d_p (Fig. 6).
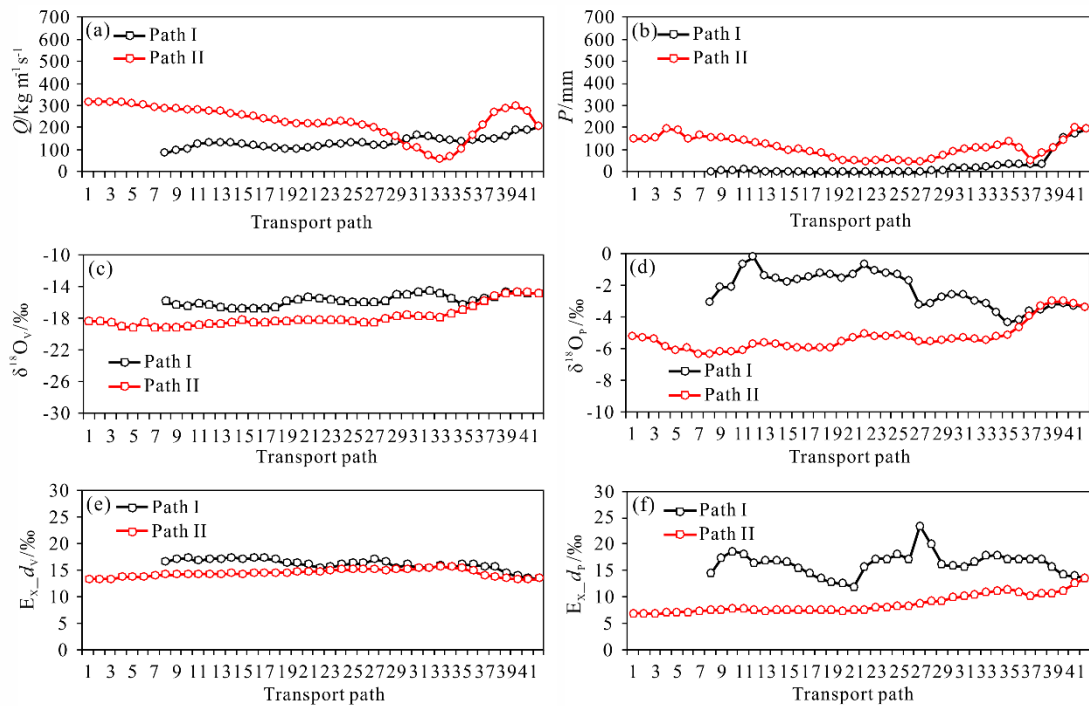
518 Fig. 6 Mean variations of Q (a), P (b), $\delta^{18}O_v$ (c), $\delta^{18}O_p$ (d), Ex_d_v (e), and Ex_d_p (f)

519 along the vapor transport paths in April.

520 Along Path I, both the Q and P showed slight increases compared to the situations

521 in January (Figs. 6a and 6b), with the average values in the first half of the water vapor

transport path before entering the Dongting Lake Basin were 128.2~~3~~ kg m^{-1} s^{-1} and 10.5 mm, respectively, still at relatively low levels. After entering the Dongting Lake Basin, the average Q and P increased to 180.1~~3~~ kg m^{-1} s^{-1} and 135.0 mm, respectively. Under the transport of latitudinal water vapor, the $\delta^{18}O_v$ increased slightly from −15.8~~3~~‰ to −14.8~~5~~9‰, while the $\delta^{18}O_p$ decreased slightly from −2.0~~6~~1‰ to −3.2~~8~~3‰ (Figs. 6c and 6d). The corresponding Ex_d$_v$ decreased from 16.4~~5~~5‰ to 14.2~~6~~3‰, and the Ex_d$_p$ decreased from 16.6~~0~~‰ to 1~~4.97~~5.0‰, indicating the input of oceanic water vapor (Figs. 6e and 6f).

Along Path II, both the Q and P were significantly larger than those along the latitudinal Path I (Figs. 6a and 6b), with the average values before entering the Dongting Lake Basin were 226.6 kg m^{-1} s^{-1} and 108.2 mm, respectively. After entering the Dongting Lake Basin, these values increased to 269.2 kg m^{-1} s^{-1} and 148.6 mm, respectively. The area where Q decreased significantly corresponds to a water vapor divergence region at the southwest corner of the Indochinese Peninsula. Under the meridional water vapor transport, the $\delta^{18}O_v$ increased from −18.2~~1~~‰ to −14.8~~6~~9‰, while the $\delta^{18}O_p$ from −5.5~~0~~‰ to −3.1~~5~~2‰ (Figs. 6c and 6d); correspondingly, the Ex_d$_v$ decreased from 14.6~~1~~‰ to 13.5~~0~~‰, while the Ex_d$_p$ increased from 8.3~~2~~‰ to 11.8~~1~~‰ (Figs. 6e and 6f), following the variation rule of ~~excess~~ deuterium excess during water vapor transport—that is, as the rainout effect progressed, the heavier isotopes preferentially left the water vapor parcel or cloud during the water vapor transport processes and generated precipitation, thus resulted in subsequent precipitation having increasingly higher deuterium excess values (Vasil'chuk, 2014).

3.2.3 Average Water Vapor Transport Path in the Dongting Lake Basin in June

Based on the ERA5 reanalysis data and isoGSM2 simulation data, the spatial distributions of the average H_{500}, Q, P, $\delta^{18}O_v$, $\delta^{18}O_p$, Ex_d$_v$, and Ex_d$_p$ were respectively calculated and plotted in June (Fig. 7). At the H_{500} field (Fig. 7a), the East Asian Trough continues to stably exist in June, but the position of trough line shifted eastward over the North Pacific Ocean. The high-pressure ridge in the eastern part of the Ural Mountains weakened and shifted eastward over Lake Baikal. The rapidly intensifying western Pacific subtropical high expanded westward and northward, with its ridge line located at approximately 22~23°N, while the India-Burma Trough in the northern Bay of Bengal strengthened continuously. The atmospheric circulation ~~situation~~ conditions indicated that most of East Asia, including the south of the Yangtze River, has entered the prevailing period of summer monsoon (Fig. 7a). The warm and moist water vapor from the Arabian Sea and the Bay of Bengal driven by the India-Burma Trough as well as along the outer edge of the subtropical high from the western Pacific met the cold air moving southward behind the East Asian Trough and thus generated an extremely long rain belt spanning 20 degrees of latitude and 70 degrees of longitude from India, through the Indochinese Peninsula, to southern China until central Japan (Fig. 7b). In this rain belt, the three largest precipitation centers were located on the west coast of India, the Thai-Myanmar border region, and the Jiangnan region of China. The formation of the first two precipitation centers was related to terrain, while the formation of the precipitation center in the Jiangnan region of China was related to the convergence of warm and moist water vapor from low latitudes to this region (Fig.

566 7b).
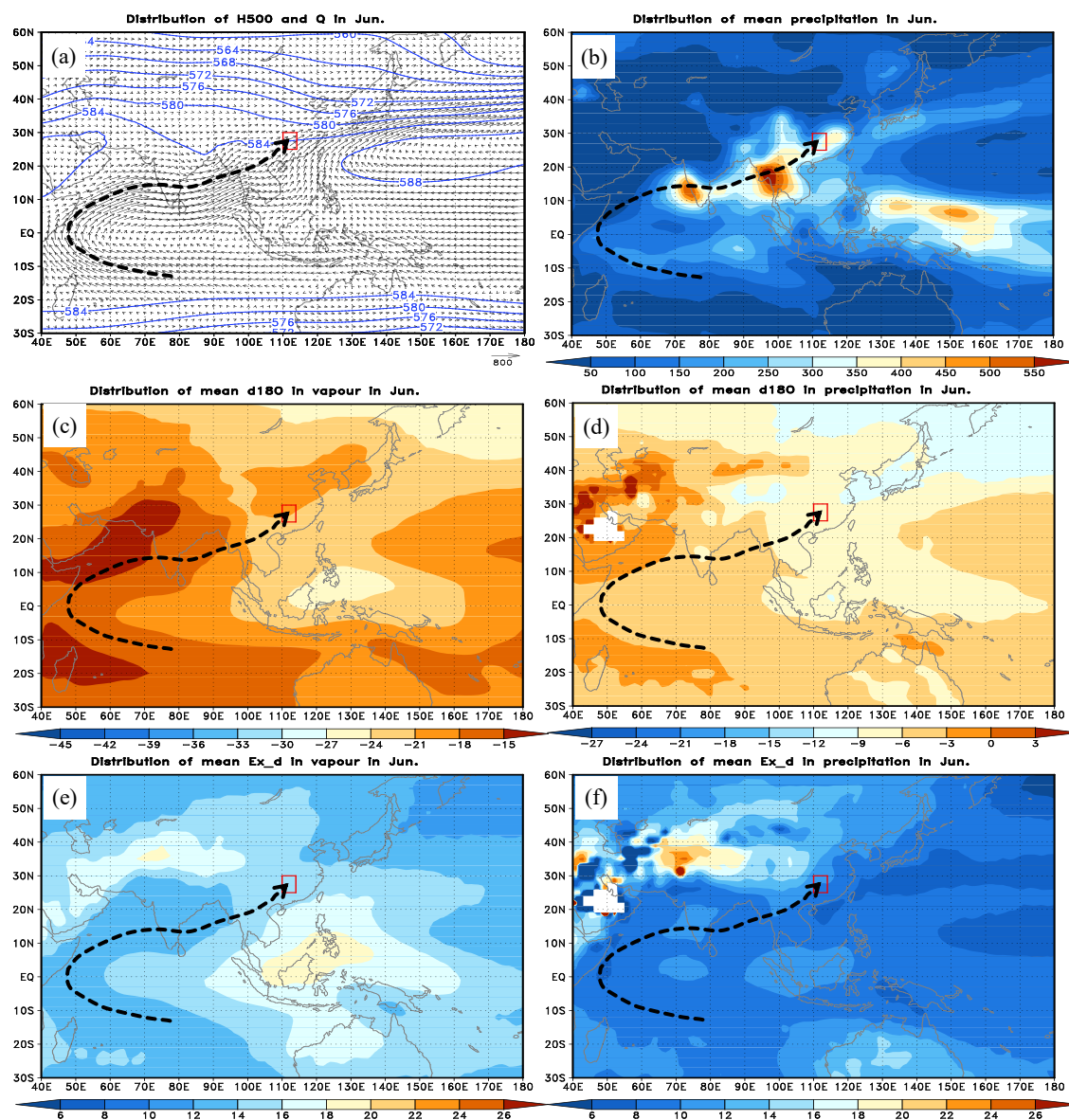
568   Fig. 7 Mean vapor transport path to the Dongting Lake Basin and the spatial

569 distributions of Q with H_{500} (a), P (b), $\delta^{18}O_v$ (c), $\delta^{18}O_p$ (d), Ex_d$_v$ (e), and Ex_d$_p$ (f) in

570   June.

571   With the change in circulation ~~situation~~condition, the distributions of the $\delta^{18}O_v$ and

572 $\delta^{18}O_p$ in June changed accordingly (Figs. 7c and 7d). The stable isotopes in both water

573 vapor and precipitation at mid-high latitudes were significantly enriched, with reduced

574 spatial differences. The $\delta^{18}O_v$ and $\delta^{18}O_p$ values remained high in the Arabian Sea, the

575   Bay of Bengal, and the Southern Ocean, the region with high $\delta^{18}O$ in the western Pacific

576   became narrowed, and the low $\delta^{18}O$ values in the Indonesia-Philippines region in the

577   western equatorial Pacific were associated with the enhanced water vapor convergence

578   (Figs. 7a, 7c, and 7d). The regional low $\delta^{18}O$ center previously present in the cold

579   season over the Tibetan Plateau had disappeared. In the Jiangnan region of China, the

580   convergence of water vapor from low-latitude oceans led to an isotopic enrichment in

581   water vapor, but the strong rainout effects caused an isotopic depletion in precipitation

582   (Figs. 7c and 7d). The spatial distributions of Ex_d_v and Ex_d_p in June showed no

583   significant differences compared to the situations in April (Figs. 5e, 5f, 7e, and 7f). The

584   high-value regions for the Ex_d_v and Ex_d_p were located in the region stretching from

585   western Asia through the Tibetan Plateau to southwestern China, as well as in the vast

586   oceanic region centered around the Philippines and Indonesia. Under the influence of

587   the summer monsoon, the difference in deuterium excess between East Asia and its

588   water vapor source—that is, the low-latitude ocean, remained relatively small (Figs. 7e

589   and 7f).

590   Based on the vector interpolation of the Q field (Fig. 7a), the water vapor transport

591   path regarding the Dongting Lake Basin as the endpoint was determined in June

592   according to the vector interpolation method introduced in Section 3.2.1 (shown by the

593   black arrow lines in Fig. 7). This water vapor transport path originated from the northern

594   branch of the South Indian Ocean subtropical high, crossed the equator, and transported

595   through the Somali Sea, the Arabian Sea, the Indian Peninsula, the Bay of Bengal, the

596   Indochinese Peninsula, and entered the southwestern region of China, finally reaching

597   the Dongting Lake Basin. It can be seen that this water vapor transport path was

598   consistent with the prevailing wind direction in June as shown in Fig. 1a. The

599   corresponding Q, P, $\delta^{18}O_v$, $\delta^{18}O_p$, Ex_d_v, and Ex_d_p along the water vapor transport

600   path were extracted, and plotted in Fig. 8.

601
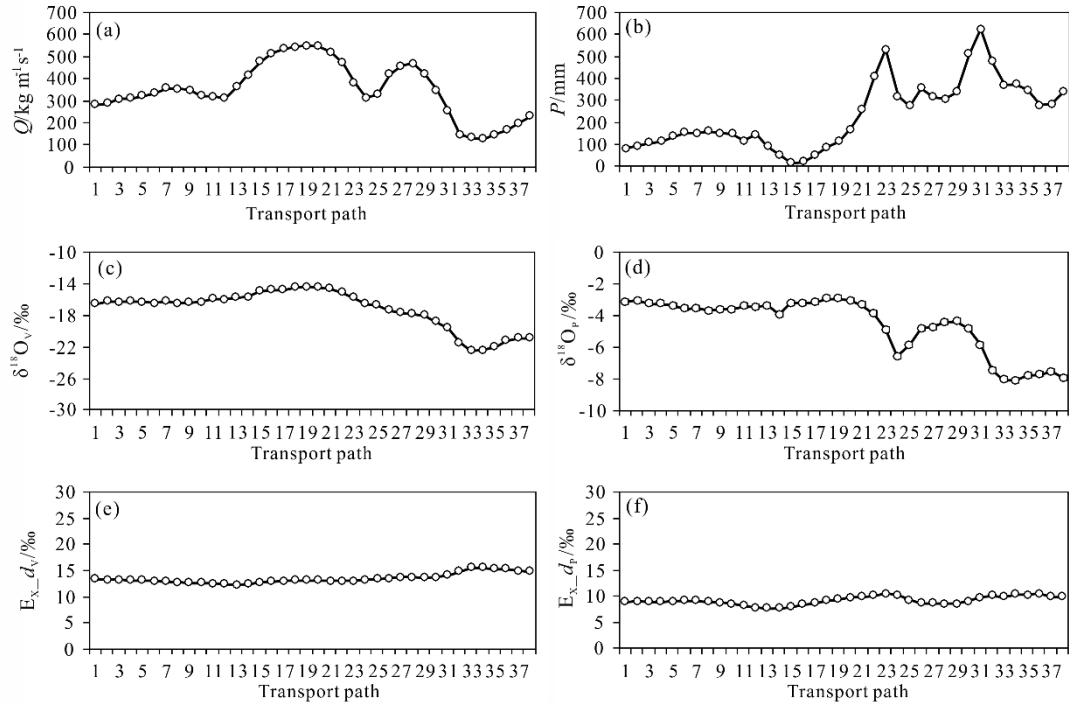
602   Fig. 8 Mean variations of Q (a), P (b), $\delta^{18}O_v$ (c), $\delta^{18}O_p$ (d), Ex_d_v (e), and Ex_d_p (f)

603   along the vapor transport path in June.

604   Along the water vapor transport path, the average Q and P were at their maximum

605   throughout the year, reaching 353.~~86~~ 9 kg m^{-1} s^{-1} and 236.5 mm, respectively (Figs. 8a

606   and 8b). The three extreme values of the Q along the transport path, or in the process

607   of transitioning from the maximum to minimum values, correspond to three P extremes

608   located at the western coast of the Indian Peninsula, the border region between Thailand

609   and Myanmar, and the region around the Dongting Lake Basin (Fig. 7b), with the values

610   of the three P extremes of 535.1 mm, 627.8 mm, and 341.5 mm, respectively (Fig. 8b).

With continuous precipitation especially after experiencing heavy precipitation and the simultaneous persistent rainout processes, the stable isotopes in both water vapor and precipitation exhibit a trend of continuous depletion (Figs. 8c and 8d). However, ~~due to continuous water vapor supply from low-latitude oceans,~~ there were no significant changes in both the Ex_d_v and Ex_d_p (Figs. 8e and 8f), the reasons may be due to the continuous water vapor supply from low-latitude oceans, similar advective paths between the grid points, and the similar degrees of sub-cloud evaporation.

3.2.4 Average Water Vapor Transport Path in the Dongting Lake Basin in October

The spatial distributions of the average H_{500}, Q, P, $\delta^{18}Ov$, $\delta^{18}Op$, Ex_d_v, and Ex_d_p in October were shown in Fig. 9. A notable feature at the H_{500} field in October was the expansion of the latitudinal westerlies toward lower latitudes (Fig. 9a). In East Asia, westerly winds prevail in the inland regions north of approximately 30°N, while much of the regions south of 30°N were still influenced by the subtropical high-pressure system. Compared to the peak period, the West Pacific subtropical high had significantly weakened in autumn, and its main body had also retreated to the open sea. However, a mesoscale anticyclone split from the high still controlled the Jiangnan region of China including the Dongting Lake Basin, creating a climate characterized by clear and crisp autumn (Fig. 9a). Due to the disappearance of the India-Burma Trough and influenced by the anticyclone circulation, the water vapor transport from the southwest low-latitude oceans decreased significantly. In the Dongting Lake Basin, both the meridional and latitudinal water vapor transport were even less than the values in January (Fig. 3a and 9a; Xiao et al., submitted). Apart from the autumn rains in

western China, precipitation was generally scarce in East Asia in this period, with the

rain belt shifting southward to lower latitudes corresponding to the convergence zone

near the equator, with the largest precipitation regions located respectively south of the

Equator in the Indian Ocean, the Malay Peninsula, and north of the Equator in the

western Pacific (Fig. 9b).
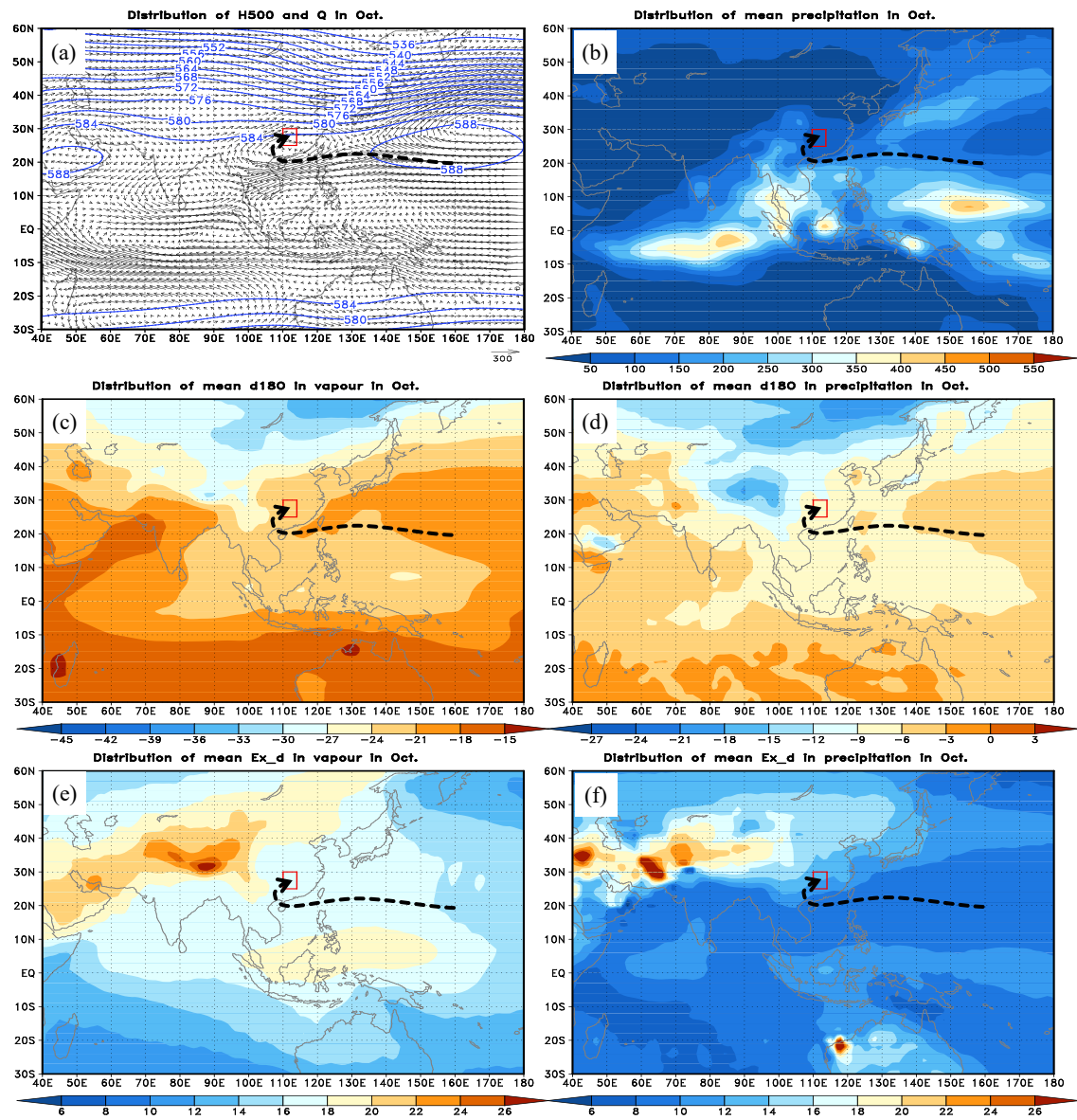
Fig. 9 Mean vapor transport path to the Dongting Lake Basin and the spatial

distributions of Q with H_{500} (a), P (b), $\delta^{18}O_v$ (c), $\delta^{18}O_p$ (d), Ex_d$_v$ (e), and Ex_d$_p$ (f) in

October.

Compared to the situations in June, there were no significant changes in the spatial distribution of the $\delta^{18}O_v$ and $\delta^{18}O_p$ in October, but their differences between land and sea as well as between high and low latitudes increased largely (Figs. 9c and 9d). The stable isotopes in water vapor and precipitation were significantly depleted in Eastern Siberia and the Tibetan Plateau, and accompanied by expansion of ranges. As a result, the $\delta^{18}O_v$ and $\delta^{18}O_p$ showed a significant decrease in the inland regions north of approximately 30°N, but unchanging in most regions south of 30°N. From the spatial distributions in October, both the Ex_d_v and Ex_d_p over the ocean or on land showed increases with varying degrees (Figs. 9e and 9f). The high-value regions of the Ex_d_v were distributed along a line from the Arabian Peninsula, West Asia, the Tibetan Plateau, to Eastern Siberia, with the maximum value located in the Tibetan Plateau. The high-value region of Ex_d_p was distributed from the Arabian Peninsula, West Asia, the Tibetan Plateau, to the Yunnan-Guizhou Plateau. With the weakening of the summer monsoon, the Ex_d_v and Ex_d_p were not significantly different in East Asia including the Dongting Lake Basin from those in the surrounding oceans.

Based on the vector interpolation of the Q field (Fig. 9a), the water vapor transport path ~~regarding the Changsha site as the endpoint~~ was determined in October according to the method introduced in section 3.2.1 (indicated by the black arrow line in Fig. 9). This water vapor transport path originated from the western Pacific, passed through the South China Sea, flowed westward along the easterly jet located in the south of the West Pacific Subtropical High and of the anticyclonic circulation over the Jiangnan region in China, and finally entered the Dongting Lake Basin bypassing the southwest

664 of the anticyclone. Although this water vapor path belonged to the latitudinal transport,

665 the water vapor source originated from the low-latitude oceans of the western Pacific.

666 The corresponding Q, P, $\delta^{18}O_p$, $\delta^{18}O_v$, Ex_d$_v$, and Ex_d$_p$ along the water vapor

667 transport path were derived in October (Fig. 10). Under the stable atmospheric

668 circulation conditions, the average water vapor flux steadily decreased from

669 approximately 299.0 kg m^{-1} s^{-1} in the source region to 168.0 kg m^{-1} s^{-1} along the water

670 vapor transport path, and further below 100.0 kg m^{-1} s^{-1} after entering the Dongting Lake

671 Basin (Fig. 10a). The P values changed gradually along the water vapor transport path,

672 decreasing from the initial approximately 145 mm to below 100 mm in the Dongting

673 Lake Basin, and further to 60.5 mm in the Changsha region (Fig. 10b). Both the $\delta^{18}O_v$

674 and $\delta^{18}O_p$ values showed slow decreases as the ranges within 2.0‰ and 1.0‰

675 respectively (Figs. 10c and 10d). The Ex_d$_v$ showed minor fluctuation, stabilizing at

676 approximately 16.8‰, while the corresponding Ex_d$_p$ remained around 8.6~~2~~‰ before

677 entering the Dongting Lake Basin. Due to the replenishment from the surface

678 evaporation, the Ex_d$_p$ values increased to 11.6~~0~~‰ after entering the Dongting Lake

679 Basin (Figs. 10e and 10f).
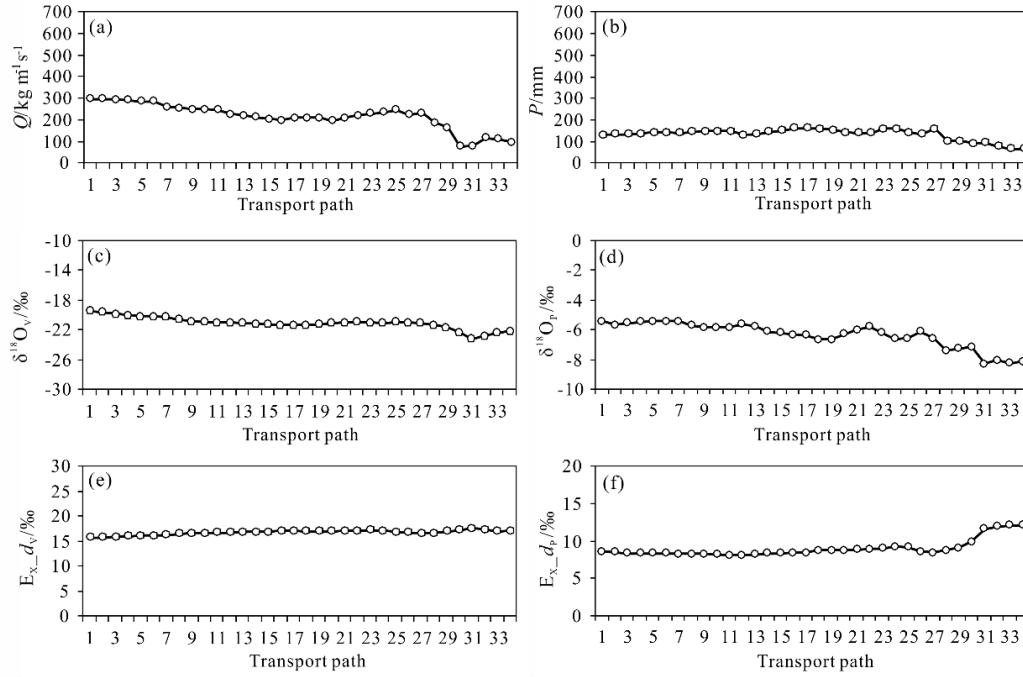
Fig. 10 Mean variations of Q (a), P (b), $\delta^{18}O_v$ (c), $\delta^{18}O_p$ (d), Ex_d_v (e), and Ex_d_p (f)

along the vapor transport path in October

4. Discussion

4.1 The Influences of the Seasonality in Water Vapor Sources on the Precipitation Isotopes.

The comparisons between the Q and $\delta^{18}O_p$ in the representative months indicated that there seems to be no obvious correspondence between these two factors: the months with low Q would exhibit either high or low $\delta^{18}O_p$, e.g. January and October, respectively (Figs. 3 and 9). Similarly, the months with high Q would exhibit either low or high $\delta^{18}O_p$, for example, June and April, respectively (Figs. 5 and 7). It has been found that regardless of the season, the precipitation in the Dongting Lake Basin mainly originated from warm and moist water vapor in low latitudes (Figs. 3, 5, 7, and 9). Therefore, whether the water vapor isotopes at the source regions and along the transport path influence the downstream isotopes of precipitation or water vapor? To

695 reveal this causality, after considering the water vapor transport paths and the air mass

696 properties of water vapor in the representative months, the water vapor regions

697 corresponding to the Arabian Peninsula (40°E~56°E, 16°N~28°N), the Arabian Sea

698 (56°E~74°E, 10°N~20°N), the Bay of Bengal (80°E~98°E, 8°N~18°N), and the

699 western Pacific Ocean (120°E~160°E, 6°N~20°N), along with the— inland regions of

700 Dongting Lake Basin (110°E~114°E, 25°N~30°N), and the inland regions of East Asia

701 monsoon region (110°E~135°E, 42°N~55°N) were labeled as Regions I, II, III, IV, V,

702 and VI, respectively (Fig. 11). The average $\delta^{18}O$ and Ex_d of water vapor and

703 precipitation for each representative region were calculated in January, April, June, and

704 October, respectively. Since the seasonal variations in the $\delta^{18}O_v$ were similar to that in

705 $\delta^{18}O_p$, Table 1 only provided the average $\delta^{18}O$ and Ex_d of water vapor for each

706 representative region.
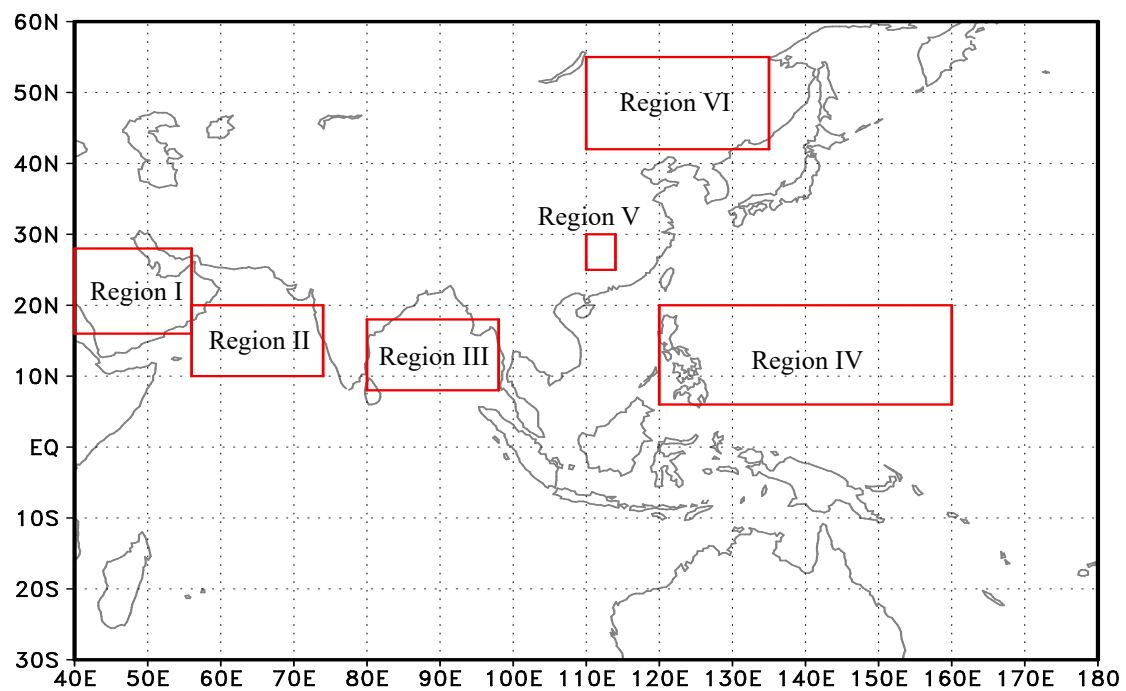
708 Fig. 11 Geographical distribution of representative regions

709 (Region I: Arabian Peninsula, Region II: Arabian Sea, Region III: Bay of Bengal,

Region IV: Western Pacific, Region V: Dongting Lake Basin, Region VI: Inland of the

East Asian monsoon region at middle and high latitudes)

Not only in Regions I to V located at mid to low latitudes but also in Region VI

located in the mid to high latitude inland regions, there ~~were~~ was significant seasonality

~~variations~~ in the average $\delta^{18}O_v$ and Ex_d_v (Table 1). The seasonal range~~seasonal~~

~~difference~~s in the $\delta^{18}O_v$ (the differences between the monthly maximum and minimum

values) in these six representative regions were 2.94‰, 3.34‰, 4.~~19~~2‰, 5.0~~6~~1‰,

7.~~18~~2‰, and 18.94‰, respectively, with the largest seasonal range~~seasonal difference~~

in $\delta^{18}O_v$ appeared in Region VI (Table 1). Except for Region VI, the minimum values

of the monthly $\delta^{18}O_v$ in other representative regions, all occurred in October, while the

maximum or second maximum values occurred in April. The seasonal range~~seasonal~~

~~difference~~s in the Ex_d_v in these six representative regions were 4.~~69~~7‰, 5.4~~2~~‰,

3.~~56~~6‰, 3.8~~1~~‰, 3.~~59~~6‰, and 9.3~~1~~‰, respectively, with the largest seasonal

range~~seasonal difference~~ in the Ex_d_v still in Region VI. Except for Region VI, the

maximum values of monthly Ex_d_v in other representative regions mostly occurred in

October, while the minimum or second minimum values occurred in April or June

(Table 1). These results indicated significant differences in water vapor isotopes

between Region VI and other oceanic or continental representative regions,

simultaneously, it can be found that oceanic water vapor had varying degrees of impact

on the isotopic composition of water vapor and precipitation in Region VI and Region

V, both located within the East Asian monsoon region, across different seasons. With

emphasis, the numeric comparisons above can also be used to determine whether the

major source of water vapor is oceanic or continental, especially based on the judgment of excess deuterium values (i.e. Ex_d$_v$), because the water vapor coming from the Arabian Peninsula in winter (Fig. 3) had relatively high Ex_d$_v$ values (Table 1, Region I), while the large amount of water vapor coming from the oceanic representative regions in summer (Fig. 7) had very low Ex_d$_v$ values (Table 1, Region III). These different sources of water vapor were ultimately reflected in their impact on the isotopic composition of precipitation in the Dongting Lake Basin.

Table 1 Mean $\delta^{18}O_v$ and Ex_d$_v$ for representative regions in the representative months

Factors	Months	Region I	Region II	Region III	Region IV	Region V	Region VI
$\delta^{18}O_v$ /‰	January	−19.041	−17.42	−18.72	−17.24	−18.82	−40.93
	April	−16.22	−15.788	−17.83	−17.94	−14.91	−28.70
	June	−17.10	−14.455	−18.10	−21.92	−20.778	−
	October	−19.162	−17.798	−22.02	−22.30	−22.091	−29.32
Ex_d$_v$ /‰	January	18.455	18.51	17.22	14.394	15.21	23.20
	April	16.93	17.465	17.03	13.91	13.556	15.64
	June	16.04	13.091	13.984.0	16.253	15.03	13.899
	October	20.73	17.33	17.54	17.72	17.14	18.293

FurthermoreAccording to the statistics in Table 1, in January, the average $\delta^{18}O_v$ and Ex_d$_v$ were −19.04‰ and 18.45‰, respectively, in Region I under the latitudinal water vapor transport, while −18.82‰ and 15.21‰, respectively, in Region V with their differences only 0.22‰ and 3.24‰, respectively; In April, the average $\delta^{18}O_v$ and Ex_d$_v$ were −16.22‰ and 16.93‰, respectively, in Region I also under the latitudinal water vapor transport, while −17.94‰ and 13.91‰, respectively, in Region IV under the meridional water vapor transport, and −14.91‰ and 13.55‰, respectively, in Region

, bFurtherly, by comparing the water vapor isotopes in Region V with those in Region VI, it can be found that although both regions were all located in the East Asian monsoon region, there were differences in the seasonal variations of water vapor isotopes (Table 1; Fig. 11). For instance, the average $\delta^{18}O_v$ in Regions V and VI in all of the representative months were −19.152‰ and −30.24‰, respectively, with a difference of 11.091‰. Moreover, the average $\delta^{18}O_v$ of these two regions showed the largest differences with a value of 22.11‰ in January, which represented the peak of the winter monsoon, while in June which represented the peak of the summer monsoon, the difference was only 1.22‰. The water vapor isotopes in Region V were consistently enriched compared to those in Region VI. The average Ex_d$_v$ in Regions V and VI in all of the representative months were 15.23‰ and 17.768‰, respectively, with a difference of −2.52‰, which was not too large. The difference was largest in January, reaching −7.998.0‰, while in June, the difference was only 1.14‰, indicating that the water vapor sources during the summer monsoon were similar in these two regions

769 (Table 1).

770   The above results about the water stable isotope differences between the

771 representative regions conform to the latitudinal and continental effects of water stable

772 isotopes and follow the law of material migration, which states that the composition of

773 water stable isotopes becomes more depleted with increasing latitude and water vapor

774 transport from high to low value regions (Feng et al., 2009; Zhang et al., 2012; Zhang

775 et al., 2016). With emphasis, for the water vapor source of precipitation in the Dongting

776 Lake Basin, the oceanic representative regions located at low latitudes may not

777 necessarily be the initial water vapor source regions, and the relationship between

778 upstream and downstream regions may not entirely be point-to-point, as there were

779 continuous water recycling and rainout processes along the water vapor transport path

780 (Pokam et al., 2012; Risi et al., 2013; Christner et al., 2018).

781   However, through the comparisons above, it can be observed that the influences

782 of upstream regions on the water vapor amount and water vapor isotopes in downstream

783 regions during water vapor transport were significant. For instance, two distinct water

784 vapor transport paths were identified in April (Fig. 5), thus it is crucial to assess which

785 path exerted a more significant influence on the isotopic composition of precipitation

786 in the Dongting Lake Basin, with priority given to the path whose air parcel isotopic

787 signature closely matches the precipitation isotopes in the basin before entry. According

788 to this principle and referring to Table 1, we observed that in April, the average $\delta^{18}O_v$

789 and Ex_d_v values of the Dongting Lake Basin (i.e. Region V) were −14.9‰ and 13.6‰,

790 respectively. Moreover, before entering the Dongting Lake Basin, the $\delta^{18}O_v$ and Ex_d_v

791 values of the air parcel on the first water vapor transport path—that is, Path I, were

792 −14.9‰ and 14.3‰, respectively (Figs. 6c and 6e). For the second transport path—that

793 is, Path II, these values were −14.9‰ and 13.5‰, respectively (Figs. 6c and 6e). Clearly,

794 the oceanic air mass with low deuterium excess had a relatively more significant impact

795 on the precipitation isotopes in April in the Dongting Lake Basin region.

4.2 Isotopic Properties of Air Masses

According to the definition of meteorology, air mass refers to a large-scale body of air over land or sea with relatively uniform horizontal physical properties such as temperature, humidity, and atmospheric stability. The horizontal extent of an air mass ranges from 10^2 km to 10^3 km, and the vertical extent ranges from 10^0 km to 10^1 km, while within the same air mass, there is little variation in temperature gradients, atmospheric vertical stability, and weather phenomena (Zhou et al., 1997). Under large-scale and relatively uniform underlying surfaces and stable atmospheric circulation conditions, water vapor and its transport belong to the characteristics of air masses or have the properties of the air mass origin regions (Dettinger, 2013; Lavers et al., 2013). Considering the sources and sinks of water vapor, the spatial distribution of water vapor isotopes is relatively similar within an air mass. In maritimeoceanic air masses, water vapor isotopes are relatively enriched, while deuterium excess of water vapor is relatively more negative, while in continental air masses, water vapor isotopes are relatively depleted, while excess deuterium excess of water vapor is relatively more negative (Rozanski et al., 1993; Araguás-Araguás et al., 1998).

With the seasonal variation in the position of the sun's orbit, the atmospheric

circulation conditions undergo seasonal variations and thus lead to the seasonality of

the air masses properties (Qian et al., 2009; Parding et al., 2016). The abundance of

water vapor isotopes at a fixed location varies due to variations in circulation conditions

(Lacour et al., 2018; Dee et al., 2018; Gou et al., 2022). In this study, the isotopic

compositions of water vapor in ~~maritime~~oceanic Regions II and IV at low latitudes and

in inland Region VI at high latitudes exhibited significant seasonal variations due to

interactions between tropical continental air masses (located in southern West Asia) and

tropical ~~maritime~~oceanic air masses, between tropical ~~maritime~~oceanic air masses and

equatorial air masses, and between temperate continental air masses and temperate

~~maritime~~oceanic air masses, respectively (Table 1; Fig. 11). In the process of seasonal

changes, as air masses move out of their source regions, their physical and weather

characteristics also change with the variations in underlying surface properties and

large-scale vertical motion conditions. East Asia is primarily controlled by modificatory

air masses, which were commonly used to describe air masses that have changed as

they move through different regions (Ding, 1990; Chang et al., 2012). Whether cold

and dry air masses moving southward or warm and moist air masses moving northward,

the isotopic composition of water vapor in the modificatory air mass continues to

become more negative, while the deuterium excess of water vapor continues to become

more positive than the original air mass, following the variation rule of stable isotope

and deuterium excess during water vapor transport (Vasil'chuk, 2014; Zhou et al., 2019;

Xu et al., 2019; Jackisch et al., 2022). In this study, interactions between modificatory

oceanic~~marine~~ air mass and modificatory continental air mass result in the water vapor

835 isotope in Region V that differed from ~~maritime~~oceanic air masses and continental air

836 masses (Table 1; Fig. 11). In summary, based on the comparison of stable isotopes of

837 water vapor and precipitation in different seasons and representative regions presented

838 in this study, it can be observed that, as an integral component of the climate system,

839 air masses in various regions not only exhibit differences in thermodynamic, dynamic,

840 hydrous, and static properties, but are also influenced by interactions between air

841 masses, the underlying surface, and the intensity of convection, among others.

842 ~~as an important member of the climate system, air mass possesses not only~~

843 ~~thermodynamic, dynamic, hydrous and static properties but also isotopic properties.~~

844 **4.3 The Difference Between Water Vapor Field and Wind Field**

845 The water vapor flux Q reflects the direction and magnitude of water vapor

846 transport in the atmosphere, while wind V reflects the direction and magnitude of the

847 movement of air particles in the atmosphere (Feng et al., 2009; Zhang et al., 2012;

848 Zhang et al., 2016). There are both differences and connections between the two factors.

849 Water vapor is transported by wind, and the wind carries water vapor from one place to

850 another, and the directions of water vapor and wind may be consistent, inconsistent, or

851 even opposite. In the East Asian monsoon region, the prevailing wind direction during

852 the summer monsoon period is generally consistent with the average water vapor

853 transport direction, both being southwest or southeast direction (Barker, et al., 2015;

854 Wu et al., 2015; Tang et al., 2015). In this study, the water vapor transport path was

855 consistent with the prevailing wind direction in June (Figs. 1a and 9). However, during

856 the winter monsoon period, the prevailing wind direction may not be consistent with

the average transport direction of water vapor—that is, the prevailing wind direction in January was northwest or northeast direction, while the average transport direction of water vapor in this period was southwest or southeast direction (Figs. 1a and 3), and supported by the water vapor transport study focusing on the Changsha region (Xiao et al., submitted).

Previous studies have shown that the most common weather systems and most precipitation events in the East Asian monsoon region are caused by cold fronts resulting from the interaction of warm and cold air masses (Chen et al., 2020). According to classical meteorological theory (Zhou et al., 1997), in a cold front system, there appears the wind from the southwest direction blows ahead of the front, and a northwest wind blows behind the front as shown in the schematic diagram in Fig. 12a. Warm and moist air from low latitudes lifts along the front and leads to rainfall, while cold and dry air from high latitudes moves southward beneath the front and lifts the warm and moist air. At different ~~altitudes~~ heights and positions, the directions of air particle movement and water vapor transport are different. For example, at ~~the~~ point A located above the warm and moist air side of the cold front surface, both air particles and water vapor are transported by southwest wind. At ~~the~~ point C located below the cold, dry air side of the cold front surface, both air particles and water vapor are transported by northwest wind. However, at ~~the~~ point B located within the front zone, the wind direction and speed are uncertain (Fig. 12b). Specifically, this front zone marked the transition from a warm air mass to a cold one, or vice versa, where meteorological factors have undergone rapid changes. Mixing between cold and warm

879 advected air could occur within this zone, manifesting as a shear zone in wind fields,

880 or as alternating southerly and northerly winds. Therefore, the dominant wind directions

881 may not always align with the average water vapor transport direction, especially in

882 frontal weather systems that dominate precipitation in the East Asian monsoon region.
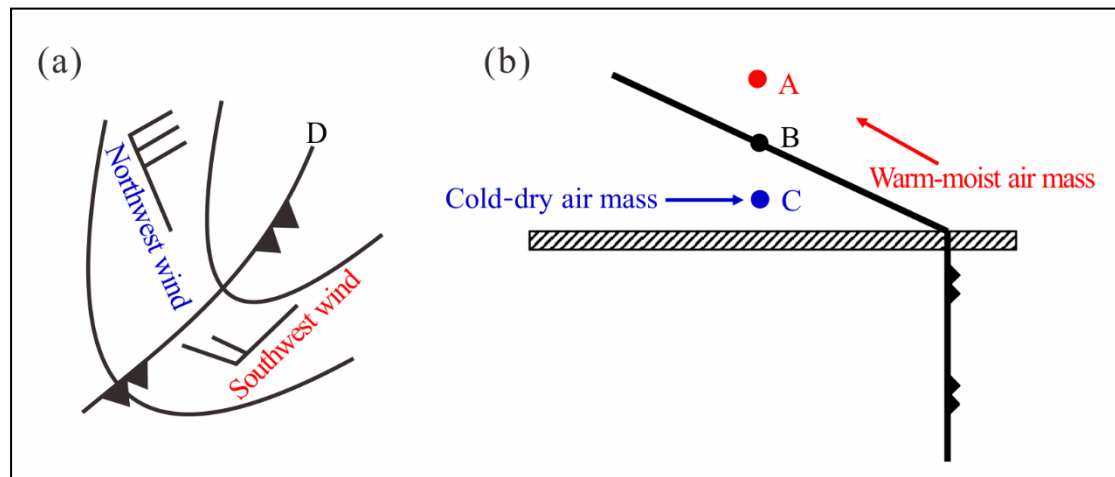
884 Fig. 12 Schematic diagram of a cold front system in East Asia (based on Zhou et al.,

885 1997).

886 **4. Conclusion**

887 Our findings revealed significant influences of water vapor source and transport

888 on precipitation isotopes in Dongting Lake Basin. Specifically, in January, water vapor

889 contributing to the Dongting precipitation originated near the Arabian Peninsula and

890 was driven by the southern branch of the westerly stream jet on the southern side of the

891 Tibetan Plateau, water vapor transported along the southern side of the Tibetan Plateau,

892 passed through southwestern China via the northern part of the Indian Peninsula, and

893 reached the Dongting Lake Basin. In April, two distinct water vapor transport paths

894 contributed to the Dongting precipitation, the first followed a trajectory similar to the

895 average water vapor transport path in January, albeit shifted slightly northward by one

degree of latitude. The second transport path, driven by the weak Western Pacific subtropical high, guided warm and moist water vapor from the low latitudes of the Western Pacific along the outer edge of the subtropical high, passing through the South China Sea and the Indochinese Peninsula and finally reached into the Dongting Lake Basin. In June, the precipitation in the Dongting Lake Basin~~Dongting precipitation~~ was influenced by a water vapor transport path originating from the northern branch of the South Indian Ocean subtropical high, crossed the equator, and transported through the Somali Sea, the Arabian Sea, the Indian Peninsula, the Bay of Bengal, the Indochinese Peninsula, and entered the southwestern region of China, finally reaching the Dongting Lake Basin. In October, the average water vapor transport path originated from the western Pacific, passed through the South China Sea, flowed westward along the easterly jet located in the south of the West Pacific Subtropical High and of the anticyclonic circulation over the Jiangnan region in China, and finally entered the Dongting Lake Basin bypassing the southwest of the anticyclone. Although this water vapor path belonged to the latitudinal transport, the water vapor source originated from the low-latitude oceans of the western Pacific. In these four months that representing different seasons, variations in the $\delta^{18}O$ and Ex_d of precipitation and water vapor along these water vapor transport paths adhered to principles of Rayleigh fractionation and water balance principles, underscoring the complex transport paths and processes that influence isotopic variations in precipitation in the Dongting Lake Basin. However, the prevailing wind direction may not be consistent with the average transport direction of water vapor, especially during the winter monsoon, which can be explained by the water

vapor field and wind field in frontal weather systems that dominate precipitation in the East Asian monsoon region.

Overall, the approach utilized in this study is grounded in fundamental meteorological theories, specifically involving water vapor diagnosis and calculations (including source regions, transport paths, and transport quantities), this analytical method is robust and has a clear physical basis. The scientific question addressed by this study is not centered on the spatial and temporal variations of water isotopes, but rather on how the seasonal variations in regional precipitation and precipitation isotopes respond to the seasonal variations in water vapor sources and transport. A potential direction for future research could be to investigate the intra-seasonal variations in composite differences across various factors, rather than focusing on inter-seasonal comparisons.

Competing interests

The authors declare that they have no known competing financial interests or personal relationships that could have appeared to influence the work reported in this paper.

Acknowledgments

This study was supported by the Natural Science Foundation of Hunan Province, China (No. 2023JJ40445) the National Natural Science Foundation of China (No. 42101130), and the Aid Program for Science and Technology Innovative Research Team in Higher Educational Institutions of Hunan Province (0531120-4944). We are grateful to the graduate students who laboriously sampled water samples without interruption and tested water stable isotopes for 13 years.

Data availability statement.

The global atmospheric reanalysis data and water stable isotope simulation data are downloaded from the ECMWF 5th generation atmospheric reanalysis data (ERA5, https://cds.climate.copernicus.eu/) and the second-generation isoGSM2 dataset (https://datadryad.org/stash/dataset/doi:10.6078/D1MM6B), respectively. The stable isotopic data of precipitation and meteorological data at the Changsha station are accessible by emailing the corresponding author (zxp@hunnu.edu.cn) with a reasonable request.

References:

Albergel, C., Dutra, E., Munier, S., Calvet, J. C., Munoz-Sabater, J., de Rosnay, P., & Balsamo, G. (2018). ERA-5 and ERA-Interim driven ISBA land surface model simulations: which one performs better?. Hydrology and Earth System Sciences, 22(6), 3515-3532.

Araguás-Araguás, L., Froehlich, K., & Rozanski, K. (1998). Stable isotope composition of precipitation over southeast Asia. Journal of Geophysical Research: Atmospheres, 103(D22), 28721-28742.

Baker, A. J., Sodemann, H., Baldini, J. U., Breitenbach, S. F., Johnson, K. R., van Hunen, J., & Zhang, P. (2015). Seasonality of westerly moisture transport in the East Asian summer monsoon and its implications for interpreting precipitation δ^{18}O. Journal of Geophysical Research: Atmospheres, 120(12), 5850-5862.

Bong, H., Cauquoin, A., Okazaki, A., Chang, E. C., Werner, M., Wei, Z., ... & Yoshimura, K. (2024). Process-Based Intercomparison of Water Isotope-Enabled

Models and Reanalysis Nudging Effects. Journal of Geophysical Research: Atmospheres, 129(1), 1-28.

Chang, C. P., Lei, Y., Sui, C. H., Lin, X., & Ren, F. (2012). Tropical cyclone and extreme rainfall trends in East Asian summer monsoon since mid-20th century. Geophysical Research Letters, 39(18), 1-7.

Chen, X., Zhang, X. Z., Zhang X. P., & Long X. (2020). Long-term Variation of Regional Extreme Precipitation in jiangnan Area and lts Possible Cause. Resources and Environment in The Yangtze Basin, 29(08),1757-1767.

Chiang, J. C., Herman, M. J., Yoshimura, K., & Fung, I. Y. (2020). Enriched East Asian oxygen isotope of precipitation indicates reduced summer seasonality in regional climate and westerlies. Proceedings of the National Academy of Sciences, 117(26), 14745-14750.

Christner, E., Aemisegger, F., Pfahl, S., Werner, M., Cauquoin, A., Schneider, M., ... & Schädler, G. (2018). The climatological impacts of continental surface evaporation, rainout, and subcloud processes on δD of water vapor and precipitation in Europe. Journal of Geophysical Research: Atmospheres, 123(8), 4390-4409.

Dahinden, F., Aemisegger, F., Wernli, H., Schneider, M., Diekmann, C. J., Ertl, B., ... & Pfahl, S. (2021). Disentangling different moisture transport pathways over the eastern subtropical North Atlantic using multi-platform isotope observations and high-resolution numerical modelling. Atmospheric Chemistry and Physics, 21(21), 16319-16347.

Dee, S. G., Nusbaumer, J., Bailey, A., Russell, J. M., Lee, J. E., Konecky, B., ... & Noone, D. C. (2018). Tracking the strength of the Walker circulation with stable isotopes in water vapor. Journal of Geophysical Research: Atmospheres, 123(14), 7254-7270.

Deng, H., Wang, Q., Zhao, Y., Zhai, J., Zhu, Y., Gui, Y., ... & Liu, K. (2024). Effect of water vapor transport and budget on precipitation in the Yangtze–Huang–Huai–Hai River Basin. Journal of Hydrology: Regional Studies, 53, 101787.

Dettinger, M. D. (2013). Atmospheric rivers as drought busters on the US West Coast. Journal of Hydrometeorology, 14(6), 1721-1732.

Ding, Y., 1990: Build-up, air mass transformation and propagation of Siberian high and its relations to cold surge in East Asia. Meteorology and Atmospheric Physics, 44, 281–292.

Esquivel-Hernández, G., Mosquera, G. M., Sánchez-Murillo, R., Quesada-Román, A., Birkel, C., Crespo, P., ... & Boll, J. (2019). Moisture transport and seasonal variations in the stable isotopic composition of rainfall in Central American and Andean Páramo during El Niño conditions (2015–2016). Hydrological Processes, 33(13), 1802-1817.

Feng, X., Faiia, A. M., & Posmentier, E. S. (2009). Seasonality of isotopes in precipitation: A global perspective. Journal of Geophysical Research: Atmospheres, 114(D8), 1-13.

Gimeno, L., Vázquez, M., Eiras-Barca, J., Sorí, R., Stojanovic, M., Algarra, I., ... & Dominguez, F. (2020). Recent progress on the sources of continental precipitation as revealed by moisture transport analysis. Earth-Science Reviews, 201, 103070.

Gou, J., Qu, S., Guan, H., Shi, P., Su, Z., Lin, Z., ... & Zhu, J. (2022). Relationship between precipitation isotopic compositions and synoptic atmospheric circulation patterns in the lower reach of the Yangtze River. Journal of Hydrology, 605, 127289, 1-15.

Guo, L., Van Der Ent, R. J., Klingaman, N. P., Demory, M. E., Vidale, P. L., Turner, A. G., ... & Chevuturi, A. (2019). Moisture sources for East Asian precipitation: Mean seasonal cycle and interannual variability. Journal of Hydrometeorology, 20(4), 657-672.

He, H., Cao, R., Wu, Z. Y., Li, Y., Yin, H., & Yuan, F. (2022). Diagnosing anomalous characteristics of atmospheric water cycle structure during seasonal-scale drought events: A case study in middle and lower reaches of Yangtze River. Water Science and Engineering, 15(2), 103-113.

Hoffmann, L., Günther, G., Li, D., Stein, O., Wu, X., Griessbach, S., ... & Wright, J. S. (2019). From ERA-Interim to ERA5: the considerable impact of ECMWF's next-generation reanalysis on Lagrangian transport simulations. Atmospheric Chemistry and Physics, 19(5), 3097-3124.

Hu, Q., Jiang, D., Lang, X., & Yao, S. (2021). Moisture sources of summer precipitation over eastern China during 1979–2009: A Lagrangian transient simulation. International Journal of Climatology, 41(2), 1162-1178.

1025   Huang, H., & Li, L. (2023). A Synchronous Variation Process of Tibetan Plateau Vortex

1026   and Southwest Vortex (in Chinese). Journal of Applied Meteorological Science,

1027   34(4), 451-462.

1028   Jackisch, D., Yeo, B. X., Switzer, A. D., He, S., Cantarero, D. L. M., Siringan, F. P., &

1029   Goodkin, N. F. (2022). Precipitation stable isotopic signatures of tropical cyclones

1030   in Metropolitan Manila, Philippines, show significant negative isotopic excursions.

1031   Natural Hazards and Earth System Sciences, 22(1), 213-226.

1032   Kathayat, G., Sinha, A., Tanoue, M., Yoshimura, K., Li, H., Zhang, H., & Cheng, H.

1033   (2021). Interannual oxygen isotope variability in Indian summer monsoon

1034   precipitation reflects changes in moisture sources. Communications Earth &

1035   Environment, 2(1), 1-10.

1036   Lacour, J. L., Risi, C., Worden, J., Clerbaux, C., & Coheur, P. F. (2018). Importance of

1037   depth and intensity of convection on the isotopic composition of water vapor as

1038   seen from IASI and TES δD observations. Earth and Planetary Science Letters,

1039   481, 387-394.

1040   Lai, X., Wang, Q., Huangfu, J., Jiang, X., Wang, L., Chen, W., ... & Tang, Yu. (2023).

1041   Progress in Climatological Research on the Southwest China Vortex (in Chinese).

1042   Chinese Journal of Atmospheric Sciences, 47(6), 1983-2000.

1043   Lavers, D. A., Allan, R. P., Villarini, G., Lloyd-Hughes, B., Brayshaw, D. J., & Wade,

1044   A. J. (2013). Future changes in atmospheric rivers and their implications for winter

1045   flooding in Britain. Environmental Research Letters, 8(3), 034010, 1-8.

1046   Lekshmy, P. R., Midhun, M., & Ramesh, R. (2022). Role of moisture transport from
1047   Western Pacific region on water vapor isotopes over the Bay of Bengal.
1048   Atmospheric Research, 265, 105895.

1049   Liang, Y., Zhao, K., Edwards, R. L., Wang, Y., Shao, Q., Zhang, Z., ... & Kong, X.
1050   (2020). East Asian monsoon changes early in the last deglaciation and insights into
1051   the interpretation of oxygen isotope changes in the Chinese stalagmite record.
1052   Quaternary Science Reviews, 250, 106699, 1-5.

1053   Liu, J., Song, X., Fu, G., Liu, X., Zhang, Y., & Han, D. (2011). Precipitation isotope
1054   characteristics and climatic controls at a continental and an island site in Northeast
1055   Asia. Climate Research, 49(1), 29-44.

1056   Liu, X., Yang, M., Wang, H., Liu, K., Dong, N., Wang, H., ... & Fan, W. (2023).
1057   Moisture sources and atmospheric circulation associated with the record-breaking
1058   rainstorm over Zhengzhou city in July 2021. Natural Hazards, 116(1), 817-836.

1059   Liu, Z., Zhang, X., Xiao, Z., He, X., Rao, Z., & Guan, H. (2022). The relationships
1060   between summer droughts/floods and oxygen stable isotope composition of
1061   precipitation in Dongting Lake Basin. Quaternary Science, 42(2), 472-486.

1062   Nie, Y., & Sun, J. (2022). Moisture sources and transport for extreme precipitation over
1063   Henan in July 2021. Geophysical Research Letters, 49(4), 1-10.

1064   Parding, K., Olseth, J. A., Liepert, B. G., & Dagestad, K. F. (2016). Influence of
1065   atmospheric circulation patterns on local cloud and solar variability in Bergen,
1066   Norway. Theoretical and Applied Climatology, 125, 625-639.

Pérez-Alarcón, A., Fernández-Alvarez, J. C., Sorí, R., Nieto, R., & Gimeno, L. (2023). Moisture source identification for precipitation associated with tropical cyclone development over the Indian Ocean: a Lagrangian approach. Climate Dynamics, 60(9), 2735-2758.

Pokam, W. M., Djiotang, L. A. T., & Mkankam, F. K. (2012). Atmospheric water vapor transport and recycling in Equatorial Central Africa through NCEP/NCAR reanalysis data. Climate Dynamics, 38, 1715-1729.

Pranindita, A., Wang-Erlandsson, L., Fetzer, I., & Teuling, A. J. (2022). Moisture recycling and the potential role of forests as moisture source during European heatwaves. Climate Dynamics, 58(1), 609-624.

Qian, L., Solomon, S. C., & Kane, T. J. (2009). Seasonal variation of thermospheric density and composition. Journal of Geophysical Research: Space Physics, 114(A1), 1-15.

Rao, Z., Chen, F., Cheng, H., Liu, W., Wang, G. A., Lai, Z., & Bloemendal, J. (2013). High-resolution summer precipitation variations in the western Chinese Loess Plateau during the last glacial. Scientific Reports, 3(1), 2785, 1-6.

Rao, Z., Jia, G., Li, Y., Chen, J., Xu, Q., & Chen, F. (2016). Asynchronous evolution of the isotopic composition and amount of precipitation in north China during the Holocene revealed by a record of compound-specific carbon and hydrogen isotopes of long-chain n-alkanes from an alpine lake. Earth and Planetary Science Letters, 446, 68-76.

Risi, C., Bony, S., Vimeux, F., Frankenberg, C., Noone, D., & Worden, J. (2010). Understanding the Sahelian water budget through the isotopic composition of water vapor and precipitation. Journal of Geophysical Research: Atmospheres, 115(D24), 1-23.

Risi, C., Noone, D., Frankenberg, C., & Worden, J. (2013). Role of continental recycling in intraseasonal variations of continental moisture as deduced from model simulations and water vapor isotopic measurements. Water Resources Research, 49(7), 4136-4156.

Rozanski, K., Araguás-Araguás, L., & Gonfiantini, R. (1993). Isotopic patterns in modern global precipitation. Climate change in continental isotopic records, 78, 1-36.

Sengupta, S., & Sarkar, A. (2006). Stable isotope evidence of dual (Arabian Sea and Bay of Bengal) vapour sources in monsoonal precipitation over north India. Earth and Planetary Science Letters, 250(3-4), 511-521.

Shi, X., Risi, C., Li, L., Wang, X., Pu, T., Zhang, G., ... & Kong, Y. (2022). What controls the skill of general circulation models to simulate the seasonal cycle in water isotopic composition in the Tibetan Plateau region?. Journal of Geophysical Research: Atmospheres, 127(22), e2022JD037048.

Shi, Y., Jin, Z., Wu, A., Li, G., & Li, F. (2021). Stable isotopic characteristics of precipitation related to the environmental controlling factors in Ningbo, East China. Environmental Science and Pollution Research, 28, 10696-10706.

Smirnov, V. V., & Moore, G. W. K. (1999). Spatial and temporal structure of atmospheric water vapor transport in the Mackenzie River basin. Journal of Climate, 12(3), 681-696

Sun, B., Zhu, Y., & Wang, H. (2011). The recent interdecadal and interannual variation of water vapor transport over eastern China. Advances in Atmospheric Sciences, 28, 1039-1048.

Tang, Y., Pang, H., Zhang, W., Li, Y., Wu, S., & Hou, S. (2015). Effects of changes in moisture source and the upstream rainout on stable isotopes in precipitation–a case study in Nanjing, eastern China. Hydrology and Earth System Sciences, 19(10), 4293-4306.

Vasil'chuk, Y. K. (2014). New data on the tendency and causes of deuterium excess variations during one snowfall. Doklady Earth Sciences 459(1), 1400-1403.

Wei, Z., Lee, X., Liu, Z., Seeboonruang, U., Koike, M., & Yoshimura, K. (2018). Influences of large-scale convection and moisture source on monthly precipitation isotope ratios observed in Thailand, Southeast Asia. Earth and Planetary Science Letters, 488, 181-192.

Wu, H., Fu, C., Zhang, C., Zhang, J., Wei, Z., & Zhang, X. (2022). Temporal variations of stable isotopes in precipitation from Yungui Plateau: insights from moisture source and rainout effect. Journal of Hydrometeorology, 23(1), 39-51.

Wu, H., Zhang, X., Xiaoyan, L., Li, G., & Huang, Y. (2015). Seasonal variations of deuterium and oxygen-18 isotopes and their response to moisture source for

precipitation events in the subtropical monsoon region. Hydrological Processes, 29(1), 90-102.

Xiao, Z., Zhang, X., Xiao, X., Chang, X., & He, X. (2024). The Effect of Convective/Advective Precipitation Partitions on the Precipitation Isotopes in the Monsoon Regions of China: A Case Study of Changsha. Journal of Hydrometeorology, 23(84), 581-590.

Xu, K., Zhong, L., Ma, Y., Zou, M., & Huang, Z. (2020). A study on the water vapor transport trend and water vapor source of the Tibetan Plateau. Theoretical and Applied Climatology, 140, 1031-1042.

Xu, T., Sun, X., Hong, H., Wang, X., Cui, M., Lei, G., ... & Jiang, X. (2019). Stable isotope ratios of typhoon rains in Fuzhou, Southeast China, during 2013–2017. Journal of Hydrology, 570, 445-453.

Yoshimura, K., Kanamitsu, M., Noone, D., & Oki, T. (2008). Historical isotope simulation using reanalysis atmospheric data. Journal of Geophysical Research: Atmospheres, 113(D19), 1-15.

Zhan, Z., Pang, H., Wu, S., Liu, Z., Zhang, W., Xu, T., ... & Hou, S. (2023). Determining key upstream convection and rainout zones affecting $\delta^{18}O$ in water vapor and precipitation based on 10-year continuous observations in the East Asian Monsoon region. Earth and Planetary Science Letters, 601, 117912.

Zhang, H., Cheng, H., Cai, Y., Spötl, C., Sinha, A., Kathayat, G., & Li, H. (2020). Effect of precipitation seasonality on annual oxygen isotopic composition in the area of

spring persistent rain in southeastern China and its paleoclimatic implication. Climate of the Past, 16(1), 211-225.

Zhang, X., Guan, H., Zhang, X., He, X., Zhang, W., Wang, X., & Yao, T. (2016). Comparisons and assessment on stable isotopic effects in precipitation simulated by different models. Quaternary Sciences, 36(6), 1343-1357.

Zhang, X., Sun, Z., Guan, H., Zhang, X., Wu, H., & Huang, Y. (2012). GCM simulations of stable isotopes in the water cycle in comparison with GNIP observations over East Asia. Acta Meteorologica Sinica, 26(4), 420-437.

Zhou, H., Zhang, X., Yao, T., Hua, M., Wang, X., Rao, Z., & He, X. (2019). Variation of δ^{18}O in precipitation and its response to upstream atmospheric convection and rainout: A case study of Changsha station, south-central China. Science of the total environment, 659, 1199-1208.

Zhou, S. Z. (1997). Meteorology and Climatology. Higher Education Press, Beijing, 118-222.